

# Helium abundances and its radial gradient from the spectra of H II regions and ring nebulae of the Milky Way

J. E. Méndez-Delgado<sup>1,2\*</sup>, C. Esteban<sup>1,2</sup>, J. García-Rojas<sup>1,2</sup>, K. Z. Arellano-Córdova<sup>1,3</sup> and M. Valerdi<sup>4</sup>

<sup>1</sup>*Instituto de Astrofísica de Canarias, E-38200 La Laguna, Tenerife, Spain*

<sup>2</sup>*Departamento de Astrofísica, Universidad de La Laguna, E-38206, La Laguna, Tenerife, Spain*

<sup>3</sup>*Instituto Nacional de Astrofísica, Óptica y Electrónica. Apdo. Postal 51 y 216, Puebla, Mexico*

<sup>4</sup>*Instituto de Astronomía, Universidad Nacional Autónoma de México, Apdo. Postal 70-264 Ciudad Universitaria, Mexico*

Accepted XXX. Received YYY; in original form ZZZ

## ABSTRACT

We determine the radial abundance gradient of helium in the disc of the Galaxy from published spectra of 19 H II regions and ring nebulae surrounding massive O stars. We revise the Galactocentric distances of the objects considering *Gaia* DR2 parallaxes and determine the physical conditions and the ionic abundance of He<sup>+</sup> in a homogeneous way, using between 3 and 10 He I recombination lines in each object. We estimate the total He abundance of the nebulae and its radial abundance gradient using four different ICF(He) schemes. The slope of the gradient is always negative and weakly dependent on the ICF(He) scheme, especially when only the objects with  $\log(\eta) < 0.9$  are considered. The slope values go from  $-0.0078$  to  $-0.0044$  dex kpc<sup>-1</sup>, consistent with the predictions of chemical evolution models of the Milky Way and chemodynamical simulations of disc galaxies. Finally, we estimate the abundance deviations of He, O and N in a sample of ring nebulae around Galactic WR stars, finding a quite similar He overabundance of about  $+0.24 \pm 0.11$  dex in three stellar ejecta ring nebulae.

**Key words:** ISM: abundances – H II regions – Galaxy: abundances – Galaxy: disc – Galaxy: evolution – ISM: bubbles – stars: massive – stars: Wolf-Rayet

## 1 INTRODUCTION

Although rare on Earth, helium is the second most abundant element in the Universe and constitutes about 24–25% of its baryonic mass. The vast majority of the cosmic helium was produced during the primordial nucleosynthesis phase just after the Big Bang. The fraction of primordial mass in helium,  $Y_P$ , has been determined following three different techniques. The results of *Wilkinson Microwave Anisotropy Probe* (WMAP) and Planck satellites devoted to the study of the Cosmic Microwave Background (CMB) anisotropies have obtained values between 0.245 and 0.247 assuming the Standard Big Bang Nucleosynthesis (Coc et al. 2005; Planck Collaboration et al. 2018). Studies of intergalactic clouds near pristine absorption systems along the line of sight of bright distant quasars determine upper limits of  $Y_P$  in the range 0.225 and 0.283 (Cooke & Fumagalli 2018). The last technique, based on the analysis of spectra of H II regions of metal-poor galaxies gives

values of  $Y_P$  between 0.238 and 0.257 in the most recent works (Izotov et al. 2014; Aver et al. 2015; Peimbert et al. 2016; Fernández et al. 2018; Valerdi et al. 2019).

After the Big Bang, helium is produced by hydrostatic nucleosynthesis in the interior of stars of all initial masses. Low-mass stars produce this element through the proton-proton chain while intermediate mass and massive ones via the CNO cycle. Helium can be also efficiently destroyed in stellar interiors by the triple-alpha process. The amount of this element that is actually ejected by a given star and enrich the ISM depends on its initial mass and the importance of stellar winds.

The analysis of Galactic H II region spectra indicates the presence of radial gradients of the abundances of heavy elements – such as O, N, Ne, S, Ar or Cl – along the disc of the Milky Way (e.g. Shaver et al. 1983; Deharveng et al. 2000; Rudolph et al. 2006; Balser et al. 2011; Esteban & García-Rojas 2018). The form of such gradients reflects the action of stellar nucleosynthesis, the distribution and history of star formation and gas flows in the chemical evolution of the Galaxy. Although the helium abun-

\* E-mail: jemd@iac.es

dance should increase with the metallicity, there is not a clear evidence of the presence of a radial gradient of this element in the Milky Way. Some authors (e.g. Peimbert et al. 1978; Talent & Dufour 1979) find a slight or marginal evidence of a negative gradient but others find a flat distribution of the helium abundance along the Galactic disc (e.g. Shaver et al. 1983; Fernández-Martín et al. 2017, see §4 for further discussion).

There are several sources of uncertainty in the determination of the total abundance of helium. The most important one is related to the ionization structure of the nebulae. The spectrum of normal H II regions only shows recombination lines of He<sup>+</sup>. Since the ionization potential of He<sup>0</sup> is 24.6 eV, we expect the presence of neutral helium in the H II region, but it cannot be observed. To determine the total helium abundance from the measured He<sup>+</sup>/H<sup>+</sup> ratio, we have to rely on an ionization correction factor, ICF. In the absence of a tailored photoionization model for the object, we have to assume a particular ICF scheme based on the results of grids of photoionization models or on the similarity of ionization potentials of other particular ions. All ICF schemes are parameterized by the ionization degree measured in the nebular spectrum. There are several ICF schemes for helium available in the literature and based on different ionic ratios (e.g. Peimbert & Torres-Peimbert 1977; Peimbert et al. 1992; Kunth & Sargent 1983; Zhang & Liu 2003).

There are two more additional sources of uncertainty in the determination of the total abundance of helium and they are related to deviations from the pure recombination spectrum of He I. The He I atom has two different level states depending on its total spin quantum number, singlets and triplets. While – in principle – the intensity ratios of singlet lines should follow the predictions of recombination theory, the triplet spectrum is affected by the metastability of the lowest triplet level, the 2<sup>3</sup>S (Osterbrock & Ferland 2006). This metastable level produces important collisional and self-absorption effects. Collisions with free electrons may pump electrons from 2<sup>3</sup>S to upper levels, enhancing the intensities of the lines coming from those excited levels with respect to the predictions of recombination theory. Although triplet lines are the most affected, some singlet lines can be also enhanced (Sawey & Berrington 1993; Kingdon & Ferland 1995). Photons of transitions ending on 2<sup>3</sup>S can be reabsorbed, and, eventually, emitted as other He I lines. This self-absorption process increases or decreases line intensities of triplet lines with respect to recombination according to the line considered. The strength of collisional effects on the He I spectrum depends on the electron density and temperature of the ionized gas, being higher in denser and hotter nebulae. The calculations of the recombination spectrum of He I performed by Porter et al. (2012) include the collisional effects in the level populations of He<sup>0</sup>. Self-absorption effects depend mostly on density, and are not expected to be very important in H II regions (Benjamin et al. 2002).

The aim of this paper is to explore the existence of a radial gradient of helium in the Milky Way using the best dataset of deep spectra of H II regions available to date and considering revised distances of the nebulae. The selection gives priority to deep spectra that have been treated homogeneously in their reduction process. The structure of this paper is as follows. In §2 we describe the sample of H II region

spectra used and the determination of the revised distances. In §3 we present the values of physical conditions, electron density and temperature –  $n_e$  and  $T_e$  – adopted for each object; the He<sup>+</sup> and He abundance recalculations, as well as discuss the different ICFs used. In §4 we discuss the results pertaining to the Galactic He radial gradients. In §5 we compute and discuss the abundance deviations of He, O and N with respect to the radial abundance gradients shown by a sample of Galactic ring nebulae around WR stars. Finally, in §6 we summarize our main conclusions.

## 2 OBSERVATIONAL DATA AND REVISED DISTANCES

We have used reddening corrected intensity ratios of several emission lines of 38 spectra corresponding to 24 Galactic H II regions and ring nebulae around massive stars (Wolf-Rayet, WR or O-type stars). The data have been obtained, reduced and analyzed by our group and published in Esteban et al. (2004, 2013, 2016, 2017), Esteban & García-Rojas (2018) and García-Rojas et al. (2004, 2005, 2006, 2007). We will refer this group of publications as the “set of source papers”. The spectra were obtained with the Ultraviolet Visual Echelle Spectrograph (UVES, D’Odorico et al. 2000) at the Very Large Telescope (VLT); the OSIRIS (Optical System for Imaging and low-Intermediate-Resolution Integrated Spectroscopy) spectrograph (Cepa et al. 2000, 2003) at the 10.4 m Gran Telescopio Canarias (GTC) and the Magellan Echelle (MagE) spectrograph at the 6.5m Clay Telescope (Marshall et al. 2008). The details of the observations and the instrument configurations used are described in the set of source papers.

In the set of source papers the assumed distance of the Sun to the Galactic Centre was  $R_0 = 8.0$  kpc (Reid 1993). Most of the recent determinations do not provide substantially different values of this parameter, but the precision has increased considerably. Bland-Hawthorn & Gerhard (2016) present a compilation of direct (primary), model-based and secondary determinations, proposing a best estimate for the distance to the Galactic Center of  $8.2 \pm 0.1$  kpc. We adopt this value and its uncertainty for all our calculations of the Galactocentric distance ( $R_G$ ) of the objects. The GRAVITY collaboration has published a very recent geometric distance determination of the Galactic centre black hole with 0.3% uncertainty (Gravity Collaboration et al. 2019), which is entirely consistent with 8.2 kpc.

The set of source papers give the Galactocentric distances,  $R_G$  for each object. In the case of the H II regions, Esteban et al. (2017) and Esteban & García-Rojas (2018) adopted the mean values of kinematic and stellar distances given in different published references and an uncertainty corresponding to their standard deviation. In order to obtain an improved set of  $R_G$  values, we have made a revision taking into account new distance measurements based on *Gaia* parallaxes of the second data release (DR2). For M8, M16, M17, M20, M42 and NGC 3576 we have adopted the distances derived by Binder & Povich (2018) from *Gaia* parallaxes, with typical uncertainties in the range 0.1-0.3 kpc. For the rest of the objects we have searched the distances of the ionizing and/or associated star (or stars) inferred by Bailer-Jones et al. (2018) from *Gaia* DR2 data

and a distance prior that varies smoothly as a function of the Galactic coordinates of the objects according to a Galaxy model. In general, we find that distances based on *Gaia* parallaxes are very similar to those assumed previously in Esteban et al. (2017) and Esteban & García-Rojas (2018). The mean difference for the 23 objects for which the two kinds of determinations can be compared is about 9% (the median is 5%). The uncertainties in the distance of the *Gaia* parallaxes tend to be larger than about 1 kpc and larger than those quoted by Esteban et al. (2017) and Esteban & García-Rojas (2018) for objects at heliocentric distances about or larger than 5 kpc. The largest differences correspond to the the most external object of the sample (Sh 2-209, 38%), but also for the objects located at  $R_G \leq 7$  kpc, with a mean difference of about 16%.

In the case of the ring nebulae (G2.4+1.4, NGC 6888, NGC 7535, RCW 52, RCW 58, Sh 2-298 and Sh 2-308), all of them are ionized by a single well identified WR or O star and are located at heliocentric distances smaller than 5 kpc. Their distances have been taken directly from the database of Bailer-Jones et al. (2018). For the rest of the objects – for which we do not have a single ionized source or lack information about their ionizing sources – we compare the distances obtained from *Gaia* DR2 data (Bailer-Jones et al. 2018) with those adopted by Esteban et al. (2017) or Esteban & García-Rojas (2018), assuming one or the other depending on which determination gives the smallest uncertainties. We describe the details for each object below.

*NGC 2579.* We analyzed the *Gaia* DR2 data for stars located within 1 arcmin around the center of the H II region. The parallaxes of the stars give a large and rather uncertain heliocentric distance for the object ( $5.31 \pm 1.01$  kpc), that corresponds to an average  $R_G$  of about  $10.88 \pm 0.78$  kpc. Copetti et al. (2007) carried out a detailed study of spectroscopic parallaxes of the possible ionizing stars of the nebula, finding a somewhat larger distance of  $R_G = 12.40 \pm 0.50$  kpc. This value is consistent with the kinematic distance derived by those authors from the  $H\alpha$  velocity field as well as the previous photometrical and kinematical determinations by Russeil et al. (2007). We assume the distance determined by Copetti et al. (2007) for this object.

*Sh 2-83.* There are not specific studies investigating the ionizing sources of this nebula. The only studies that give the distance of Sh 2-83 are those by Caplan et al. (2000) and Anderson et al. (2015) based on kinematic data of the nebular gas, and both give the same heliocentric distance of 18.4 kpc, the largest value of the whole sample. If the object is at such large distance, its parallax would be too small to be well measured in *Gaia* DR2. Therefore, it is not surprising that we do not find stars at so large distances in our analysis for stars located within 1 arcmin around the center of the H II region. We adopted the distance obtained by Caplan et al. (2000) and Anderson et al. (2015), that was the one assumed by Esteban et al. (2017) for this object.

*Sh 2-209.* Chini & Wink (1984) identified 3 ionizing stars for this nebula, indicating their position in a photograph. We have searched for those stars in the *Gaia* DR2 database obtaining  $R_G$  about 10.5 kpc for all of them. These values are very much lower than the  $17.00 \pm 0.70$  kpc adopted by Esteban et al. (2017) based on several different but consistent kinematical and spectrophotometrical deter-

minations. This is a serious drawback. The rather low O/H ratio of Sh 2-209 is more consistent with the larger value of the distance considering the predictions of the latest determinations of the Galactic O/H gradient (e.g. Esteban et al. 2017, see their Figure 11) for  $R_G \sim 10.5$  kpc. Conversely, if we accept that the object is at  $R_G = 17$  kpc, it would imply a heliocentric distance of about 9 kpc, but we do not find stars located at such large distances within 3 arcmin around the centre of the H II region in *Gaia* DR2. Such a high heliocentric distance may imply a parallax too small to be measured in *Gaia* DR2 and this may be the explanation of not finding suitable distant stars in the catalogue. We finally adopt the distance of  $17.00 \pm 0.70$  kpc given by Esteban et al. (2017) for this object.

*Sh 2-311.* This H II region is ionized by a single star: HD 64315, but it is a multiple stellar system (Lorenzo et al. 2017) and its *Gaia* parallax is negative. We obtained and represented the parallaxes and proper motions of all stars located within 5 arcmin around HD 64315 (1810 stars) finding 3 defined peaks in the distribution. We calculated the distance corresponding to the center of each peak and the uncertainty corresponding to  $1\sigma$ . We assumed the distance of  $11.22 \pm 0.22$  kpc corresponding to the peak of the most distant distribution of stars, which is very similar to that of  $11.1 \pm 0.4$  kpc assumed by Esteban et al. (2017). We assume the value determined from the *Gaia* data for this object

The rest of the sample objects are located at heliocentric distances about or larger than 5 kpc and their *Gaia* DR2 parallaxes give rather uncertain distances. We have finally assumed the distance adopted by Esteban et al. (2017) or Esteban & García-Rojas (2018) for all these nebulae. As it has been said before, this distance corresponds to the mean of several independent photometrical and kinematical determinations (obtained mainly from Caplan et al. 2000; Russeil 2003; Russeil et al. 2007; Quireza et al. 2006; Balser et al. 2011; Foster & Brunt 2015) that provide a standard deviation lower than the distance uncertainty obtained from the *Gaia* parallaxes.

*NGC 3603.* This distant object has been cited as a Galactic giant H II region and compared with 30 Doradus in the Large Magellanic Cloud. Drew et al. (2019) compiled a list of almost 300 candidate O stars of the associated cluster and estimate an heliocentric distance of  $7.0 \pm 1.0$  kpc from the *Gaia* DR2 data, that implies a  $R_G = 8.6 \pm 1.0$  kpc, in complete agreement with the distance of  $8.6 \pm 0.4$  kpc adopted by Esteban et al. (2017).

*Sh 2-100.* Samal et al. (2010) found that Sh 2-100 is in a molecular complex containing 7 H II regions. Those authors identify several ionizing stars inside the complex. We have obtained their *Gaia* parallaxes that give a very large heliocentric distance of  $9.5^{+2.4}_{-1.7}$  kpc for the object, corresponding to  $R_G = 10.2^{+2.4}_{-1.7}$  kpc, which is consistent with the value adopted by Esteban et al. (2017) but much more uncertain.

*Sh 2-127.* Rudolph et al. (1996) conclude that this H II region is ionized by two O-type stars. Only one of them is visible in the optical, that seems to be associated to the *Gaia* DR2 source 217611164377605888. The parallax of this source is very uncertain and gives a very large heliocentric distance of  $9.5^{+2.6}_{-1.9}$  kpc, that corresponds to  $R_G = 13.2^{+2.1}_{-1.6}$  kpc. This value is consistent with the distance of  $14.2 \pm 1.0$  kpc quoted by Esteban et al. (2017) within the errors.

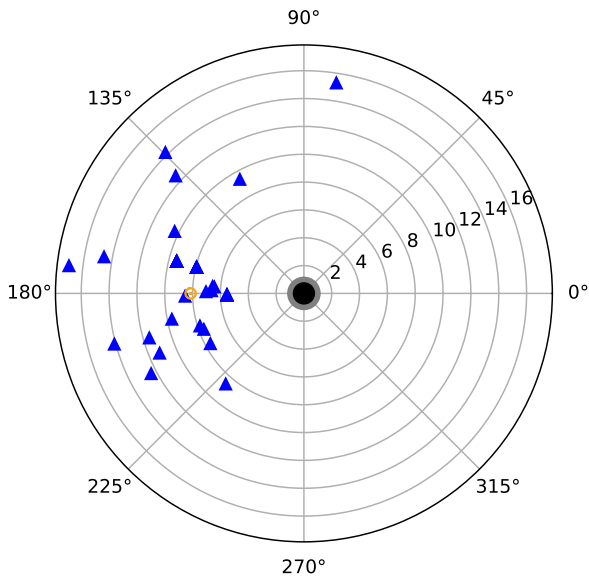


**Figure 1.** Spatial distribution of the sample nebulae (blue triangles) onto the Galactic plane with respect to the centre of the Milky Way. The concentric circles indicate increasing Galactocentric distances (in kpc). The Sun position is given by the orange small circle.

*Sh 2-128.* This H II region is ionized by the star ALS 19702 (Bohigas & Tapia 2003). Its parallax is very uncertain, due to its heliocentric distance of  $8.6^{+2.2}_{-1.6}$  kpc, corresponding to  $R_G = 12.7^{+1.8}_{-1.3}$  kpc, but entirely consistent with that of  $12.50 \pm 0.40$  kpc quoted by Esteban et al. (2017).

*Sh 2-152.* We use the star no. 4 of Russeil et al. (2007) for obtaining the *Gaia* DR2 parallax (the stars no. 1 to 3 are more likely associated with Sh 2-153), obtaining a  $R_G$  of  $10.9^{+1.6}_{-1.1}$  kpc, in agreement but slightly more uncertain than the distance of  $10.3 \pm 1.0$  kpc given by Esteban & García-Rojas (2018).

*Sh 2-212.* Moffat et al. (1979) catalogued several stars associated to this star-forming region. Their *Gaia* parallaxes are very uncertain and provide an heliocentric distance of  $6.0^{+2.2}_{-1.5}$  kpc and  $R_G = 13.9^{+2.2}_{-1.5}$  kpc, which is consistent with that of  $14.6 \pm 1.4$  kpc given by Esteban et al. (2017).

*Sh 2-288.* Avedisova & Kondratenko (1984) found that this nebulae is ionized by the star GSC 04823-00146. Its very uncertain parallax gives  $R_G = 12.7^{+1.5}_{-1.1}$  kpc. We use the more precise distance of  $14.10 \pm 0.40$  kpc quoted by Esteban et al. (2017).

In Table 1 we list the objects whose spectra are used in this paper along with their type (H II region or ring nebula around WR or O-type star), adopted  $R_G$ , instrument and telescope with which they were observed and the reference to their published spectra. In Fig. 1 we show the spatial distribution of the sample nebulae onto the Galactic plane.

### 3 RESULTS

Although the set of source papers present calculations of physical conditions – electron temperature,  $T_e$ , and density,  $n_e$  – and ionic and total abundances of several elements – including helium in some cases – for the nebulae, we decided

to re-calculate all the relevant quantities in order to have a homogeneous set of values using the same methodology and updated atomic data.

#### 3.1 Physical Conditions

The values of  $n_e$  and  $T_e$  used for the calculation of the ionic abundances of the H II regions have been taken from Arellano-Córdova et al. (2020). In the case of the ring nebulae – G2.4+1.4, NGC 6888, NGC 7635, RCW52, RCW58, Sh 2-298 and Sh 2-308 –, we recalculate their  $n_e$  and  $T_e$  using the same methodology and atomic data as for the rest of the objects. Following Arellano-Córdova et al. (2020), we use the version 1.0.26 of PYNEB (Luridiana et al. 2015) in combination with the atomic data for collisionally excited lines listed in Table 2 and the reddening corrected line-intensity ratios published in the source papers. The  $n_e$  was calculated using the ratio  $[S II] \lambda 6717/\lambda 6731$  or its average with  $[O II] \lambda 3729/\lambda 3726$  when both density diagnostics were available. We obtain low densities for most of the objects, and assumed the value  $n_e = 100 \text{ cm}^{-3}$  (Osterbrock & Ferland 2006) to determine  $T_e$  and ionic abundances when  $n_e < 100 \text{ cm}^{-3}$ . We used a two-zone scheme characterized by  $T_e([N II])$  and  $T_e([O III])$  derived from the line intensity ratios  $[N II] (\lambda 6548 + \lambda 6584)/\lambda 5755$  and  $[O III] (\lambda 4959 + \lambda 5007)/\lambda 4363$ , respectively. Although the intensity of the  $[N II] \lambda 5755$  auroral line may have some small contribution due to recombination, we have not considered such effect in our calculations. We have estimated the contribution due to recombination using the formulae given by Liu et al. (2000) finding that it is almost negligible and always smaller than the uncertainties. We have used the temperature relation proposed by Esteban et al. (2009, their equation 3) – calibrated with normal and giant H II regions – to estimate  $T_e([N II])$  or  $T_e([O III])$  in those objects where one of these temperature indicators was not available. We have used Monte Carlo calculations to estimate the uncertainties associated to each value of  $n_e$  and  $T_e$ . We generated 500 random values for each diagnostic line ratio assuming a Gaussian distribution with a standard deviation equal to the associated uncertainty of the line intensities involved in the diagnostic. With these distributions, we calculated new simulated values of  $n_e$  and  $T_e$ . Their associated errors correspond to a deviation of 68 percent – equivalent to one standard deviation – centred in the mode of the distribution. The final results for  $n_e$ ,  $T_e([N II])$  and  $T_e([O III])$  and their associated uncertainties are included in Table 3.

#### 3.2 He<sup>+</sup> abundances

All the spectra of our sample show several He I recombination lines. Although the set of source papers present calculations of the He<sup>+</sup>/H<sup>+</sup> and He/H ratios of some of the nebulae, we have re-calculated them using the physical conditions indicated in Section 3.1. For each object, we use all or several of the following list of He I lines:  $\lambda 3614$ ,  $\lambda 3889$ ,  $\lambda 3965$ ,  $\lambda 4026$ ,  $\lambda 4121$ ,  $\lambda 4388$ ,  $\lambda 4438$ ,  $\lambda 4471$ ,  $\lambda 4713$ ,  $\lambda 4922$ ,  $\lambda 5016$ ,  $\lambda 5048$ ,  $\lambda 5876$ ,  $\lambda 6678$ ,  $\lambda 7065$ ,  $\lambda 7281$  and  $\lambda 9464$ . The He<sup>+</sup> abundance has been determined using PYNEB, the aforementioned line intensity ratios taken from the set of source papers, the values of  $n_e$  and  $T_e([O III])$  given in Table 3 and the effective recombination coefficient computations by Porter et al. (2012,

**Table 1.** Sample of objects which spectroscopical data are used in this paper.

Object	Type <sup>a</sup>	$R_G$ (kpc)	Telescope	Instrument	Reference
G2.4+1.4	WR-RN	$5.53^{+0.32}_{-0.29}$ <sup>b</sup>	GTC MTC	OSIRIS MagE	Esteban et al. (2016)
M8	H II	$7.04 \pm 0.20$ <sup>b</sup>	VLT	UVES	García-Rojas et al. (2007)
M16	H II	$6.58 \pm 0.28$ <sup>b</sup>	VLT	UVES	García-Rojas et al. (2006)
M17	H II	$6.46 \pm 0.26$ <sup>b</sup>	VLT	UVES	García-Rojas et al. (2007)
M20	H II	$6.64 \pm 0.31$ <sup>b</sup>	VLT	UVES	García-Rojas et al. (2006)
M42	H II	$8.54 \pm 0.11$ <sup>b</sup>	VLT	UVES	Esteban et al. (2004)
NGC 2579	H II	$12.40 \pm 0.50$ <sup>c</sup>	VLT	UVES	Esteban et al. (2013)
NGC 3576	H II	$7.64 \pm 0.30$ <sup>b</sup>	VLT	UVES	García-Rojas et al. (2004)
NGC 3603	H II	$8.60 \pm 0.40$ <sup>c</sup>	VLT	UVES	García-Rojas et al. (2006)
NGC 6888	WR-RN	$7.94 \pm 0.16$ <sup>b</sup>	GTC	OSIRIS	Esteban et al. (2016)
NGC 7635	O-RN	$9.43^{+0.21}_{-0.20}$ <sup>b</sup>	GTC	OSIRIS	Esteban et al. (2016)
RCW 52	O-RN	$7.83^{+0.21}_{-0.10}$ <sup>b</sup>	MTC	MagE	Esteban et al. (2016)
RCW 58	WR-RN	$7.63^{+0.50}_{-0.42}$ <sup>b</sup>	MTC	MagE	Esteban et al. (2016)
Sh 2-83	H II	$15.30 \pm 0.10$ <sup>c</sup>	GTC	OSIRIS	Esteban et al. (2017)
Sh 2-100	H II	$9.40 \pm 0.30$ <sup>c</sup>	GTC	OSIRIS	Esteban et al. (2017)
Sh 2-127	H II	$14.2 \pm 1.0$ <sup>c</sup>	GTC	OSIRIS	Esteban et al. (2017)
Sh 2-128	H II	$12.50 \pm 0.40$ <sup>c</sup>	GTC	OSIRIS	Esteban et al. (2017)
Sh 2-152	H II	$10.3 \pm 1.0$ <sup>c</sup>	GTC	OSIRIS	Esteban & García-Rojas (2018)
Sh 2-209	H II	$17.00 \pm 0.70$ <sup>c</sup>	GTC	OSIRIS	Esteban et al. (2017)
Sh 2-212	H II	$14.6 \pm 1.4$ <sup>c</sup>	GTC	OSIRIS	Esteban et al. (2017)
Sh 2-288	H II	$14.10 \pm 0.40$ <sup>c</sup>	GTC	OSIRIS	Esteban et al. (2017)
Sh 2-298	WR-RN	$11.56^{+0.87}_{-0.65}$ <sup>b</sup>	VLT	UVES	Esteban et al. (2017)
Sh 2-308	WR-RN	$9.67^{+0.31}_{-0.27}$ <sup>b</sup>	MTC	MagE	Esteban et al. (2016)
Sh 2-311	H II	$11.22 \pm 0.22$ <sup>b</sup>	VLT	UVES	García-Rojas et al. (2005)

<sup>a</sup> H II: H II region; WR-RN: Wolf-Rayet ring nebula; O-RN: ring nebula around O-type star.

<sup>b</sup> Distance determined from *Gaia* DR2 parallaxes (see text for details).

<sup>c</sup> Distance taken from Esteban et al. (2017) or Esteban & García-Rojas (2018).

**Table 2.** Atomic dataset used for collisionally excited lines of selected heavy-element ions.

Ion	Transition probabilities and energy levels	Collisional strengths
N <sup>+</sup>	Froese Fischer & Tachiev (2004)	Tayal (2011)
O <sup>+</sup>	Froese Fischer & Tachiev (2004)	Kisielius et al. (2009)
O <sup>2+</sup>	Wiese et al. (1996); Storey & Zeippen (2000)	Storey et al. (2014)
S <sup>+</sup>	Podobedova et al. (2009)	Tayal & Zatsarinny (2010)
S <sup>2+</sup>	Podobedova et al. (2009)	Grieve et al. (2014)

2013) for He I lines and Storey & Hummer (1995) for H I lines. The calculations by Porter et al. (2012) include collisional effects in the level populations of He<sup>0</sup>. A Monte Carlo simulation similar to the one described in Section 3.1 – including random distributions of  $n_e$ ,  $T_e$  and the line intensities – was applied to estimate the uncertainty of the He<sup>+</sup>/H<sup>+</sup> ratios derived for each individual line of each spectrum. The He<sup>+</sup>/H<sup>+</sup> ratios obtained for each of the He I lines of the spectra of the sample objects are shown in Table A1. Lines with intensity uncertainties greater than 40% and those affected by blending with telluric lines or other spectral features were not considered for abundance determinations. Moreover, the He<sup>+</sup>/H<sup>+</sup> ratios calculated from the bright He I  $\lambda$ 3889 and  $\lambda$ 7065 lines are not included in Table A1. Both lines are the most affected, with great difference, by optical depth effects of the 2 <sup>3</sup>S level on the predicted recombination spectrum of He I (Benjamin et al. 2002), that only affect noticeably to triplet lines. Moreover, He I  $\lambda$ 3888.64 is blended with the

also bright H I  $\lambda$ 3889.05 line even in our highest spectral resolution spectra.

We have calculated the weighted mean of the individual He<sup>+</sup>/H<sup>+</sup> ratios of each spectrum. The weight of each line has been taken as the inverse of the square of the error associated with its He<sup>+</sup>/H<sup>+</sup> value. For a given spectrum, we have calculated means taking all possible combinations of the individual lines without repetition, leaving at least 3 lines to average (for those spectra with more than 3 He I lines). Once this is done, of all the means, we consider those within the 5th percentile of uncertainty and, from this subset, we finally select the mean for which more He I lines have been used for its calculation. This method excludes the most discrepant individual lines but maintain the largest possible number of them giving consistent values. The finally adopted mean He<sup>+</sup>/H<sup>+</sup> ratio of each spectrum is also included in Table A1. The uncertainty associated to that mean corresponds to the weighted standard deviation. In Table A2, we give the list

**Table 3.** Physical conditions and some heavy-element ionic abundances<sup>a</sup> for the sample objects.

Object	Zone	$n_e$ ( $\text{cm}^{-3}$ )	$T_e([\text{O III}])$ (K)	$T_e([\text{N II}])$ (K)	$\text{O}^+$	$\text{O}^{2+}$	$\text{S}^+$	$\text{S}^{2+}$	$\text{N}^+$
G2.4+1.4	A1	110 ± 50	8180 ± 1000 <sup>b</sup>	8780 ± 700	8.10 ± 0.26	8.64 ± 0.32	-	-	-
	A2	960 ± 160	10370 ± 990	8980 ± 350	7.90 ± 0.12	8.22 ± 0.22	6.61 ± 0.07	6.90 ± 0.13	7.36 ± 0.05
	A3	180 ± 70	13520 ± 2990	12510 ± 2090	7.50 ± 0.46	7.78 ± 0.47	-	-	-
	A4	100 ± 100	10850 ± 1350	10340 ± 1500	7.49 ± 0.44	8.22 ± 0.27	6.00 ± 0.21	6.42 ± 0.40	-
	A5	110 ± 40	9300 ± 1320 <sup>b</sup>	9560 ± 920	7.96 ± 0.30	8.43 ± 0.36	-	-	-
M8		1280 ± 480	8040 ± 90	8360 ± 110	8.35 ± 0.06	7.89 ± 0.03	6.06 ± 0.04	6.90 ± 0.02	-
M16		1120 ± 220	7600 ± 210	8320 ± 140	8.46 ± 0.06	7.92 ± 0.08	6.44 ± 0.04	6.86 ± 0.05	-
M17		470 ± 130	7970 ± 120	8900 ± 210	7.79 ± 0.07	8.45 ± 0.04	5.53 ± 0.05	6.93 ± 0.03	-
M20		260 ± 60	7760 ± 250	8260 ± 130	8.48 ± 0.05	7.74 ± 0.08	6.31 ± 0.03	6.83 ± 0.05	-
M42		6310 ± 2970	8270 ± 50	10140 ± 280	7.74 ± 0.16	8.44 ± 0.01	5.48 ± 0.16	6.85 ± 0.04	-
NGC 2579		950 ± 220	9360 ± 170	8640 ± 280 <sup>c</sup>	7.99 ± 0.09	8.20 ± 0.05	5.54 ± 0.06	6.58 ± 0.03	-
NGC 3576		1490 ± 280	8440 ± 60	8760 ± 200	8.04 ± 0.07	8.37 ± 0.02	5.79 ± 0.05	6.88 ± 0.04	-
NGC 3603		2760 ± 910	9020 ± 140	11190 ± 550	7.35 ± 0.13	8.44 ± 0.04	5.07 ± 0.10	6.88 ± 0.04	-
NGC 6888	A1	100 ± 100	19040 ± 1130	7700 ± 700	8.51 ± 0.28	7.64 ± 0.05	6.26 ± 0.11	-	-
	A2	250 ± 80	12650 ± 410	7410 ± 90	8.31 ± 0.05	7.53 ± 0.06	6.27 ± 0.03	6.09 ± 0.08	-
	A3	200 ± 80	9970 ± 660	7580 ± 110	8.13 ± 0.05	7.71 ± 0.16	6.15 ± 0.04	6.38 ± 0.20	7.74 ± 0.02
	A4	120 ± 90	10130 ± 970	8870 ± 140	7.46 ± 0.06	7.93 ± 0.22	5.53 ± 0.03	6.58 ± 0.30	8.06 ± 0.03
	A5	170 ± 70	9970 ± 550	8740 ± 260	7.47 ± 0.10	7.95 ± 0.13	5.55 ± 0.05	6.68 ± 0.18	8.01 ± 0.04
	A6	170 ± 110	9570 ± 780	8720 ± 180	7.54 ± 0.07	8.00 ± 0.20	5.54 ± 0.04	6.74 ± 0.26	7.33 ± 0.02
NGC 7635	A1	530 ± 90	7240 ± 230 <sup>b</sup>	8110 ± 160	8.32 ± 0.06	7.92 ± 0.09	6.42 ± 0.04	7.05 ± 0.13	-
	A2	120 ± 40	8030 ± 520	8040 ± 520	7.98 ± 0.21	8.29 ± 0.16	5.74 ± 0.12	7.06 ± 0.22	-
	A3	100 ± 50	7570 ± 610	8200 ± 380	8.08 ± 0.15	8.33 ± 0.25	5.84 ± 0.09	7.16 ± 0.33	-
	A4	1460 ± 150	8710 ± 420	9050 ± 90	8.14 ± 0.03	7.60 ± 0.11	6.15 ± 0.03	6.97 ± 0.15	-
	A5	190 ± 100	7280 ± 630 <sup>b</sup>	8140 ± 440	8.20 ± 0.17	8.17 ± 0.27	6.04 ± 0.10	6.96 ± 0.36	-
	A6	100 ± 100	7020 ± 710 <sup>b</sup>	7960 ± 500	8.21 ± 0.20	8.14 ± 0.31	6.11 ± 0.10	7.02 ± 0.43	-
RCW 52		230 ± 70	5910 ± 620 <sup>b</sup>	7190 ± 430	8.87 ± 0.23	8.12 ± 0.34	6.64 ± 0.14	7.30 ± 0.20	-
RCW 58		100 ± 100	4770 ± 250 <sup>b</sup>	6390 ± 180	8.36 ± 0.11	8.23 ± 0.23	6.28 ± 0.06	7.49 ± 0.14	8.43 ± 0.05
Sh 2-83		300 ± 90	10370 ± 370	11960 ± 640	7.15 ± 0.12	8.25 ± 0.07	5.20 ± 0.07	6.51 ± 0.10	-
Sh 2-100		420 ± 240	8250 ± 150	8610 ± 250	7.73 ± 0.10	8.41 ± 0.04	5.53 ± 0.07	6.96 ± 0.06	-
Sh 2-127		600 ± 100	9660 ± 220 <sup>b</sup>	9810 ± 150	8.20 ± 0.05	7.88 ± 0.21	5.91 ± 0.03	6.72 ± 0.07	-
Sh 2-128		480 ± 100	9970 ± 340	10550 ± 240	7.84 ± 0.06	7.98 ± 0.07	5.62 ± 0.04	6.56 ± 0.09	-
Sh 2-152		750 ± 80	7360 ± 120	8200 ± 70	8.46 ± 0.03	7.70 ± 0.05	6.15 ± 0.02	7.18 ± 0.06	-
Sh 2-209		300 ± 290	10760 ± 1140 <sup>b</sup>	10580 ± 800	7.67 ± 0.31	7.88 ± 0.21	5.51 ± 0.11	6.29 ± 0.29	-
Sh 2-212		100 ± 100	11250 ± 970	8350 ± 770	8.16 ± 0.31	7.81 ± 0.17	5.16 ± 0.18	5.94 ± 0.23	-
Sh 2-288		410 ± 270	9200 ± 530	9430 ± 340	8.20 ± 0.11	7.75 ± 0.15	5.93 ± 0.07	6.67 ± 0.19	-
Sh 2-298		100 ± 100	11720 ± 210	11650 ± 490	8.15 ± 0.10	8.10 ± 0.04	6.48 ± 0.06	6.50 ± 0.03	7.32 ± 0.04
Sh 2-308		100 ± 100	16600 ± 2470	14300 ± 2910	6.92 ± 0.42	7.84 ± 0.24	5.32 ± 0.26	6.53 ± 0.16	7.08 ± 0.18
Sh 2-311		290 ± 80	8940 ± 110	9270 ± 180	8.28 ± 0.06	7.83 ± 0.03	6.21 ± 0.04	6.70 ± 0.03	-

<sup>a</sup> In units of  $12 + \log(X^{n+}/\text{H}^+)$ .

<sup>b</sup>  $T_e([\text{O III}])$  estimated from  $T_e([\text{N II}])$  using equation 3 of Esteban et al. (2009).

<sup>c</sup>  $T_e([\text{N II}])$  estimated from  $T_e([\text{O III}])$  using equation 3 of Esteban et al. (2009).

of individual He I lines used to derive the average value of the  $\text{He}^+/\text{H}^+$  ratio adopted for each spectrum.

The usual methodology for calculating chemical abundances in H II regions is to consider a zone of high and low ionization and adopt a representative  $T_e$  for each zone. However, this may be inappropriate for several ions, because they can emit radiation in an intermediate zone or in both ionization zones. This is the case of  $\text{He}^+$ , since it can emit in the high and low ionization zone. To calculate  $\text{He}^+$  optimally, the characteristic temperature of the ion –  $T_e(\text{He I})$  in this case – should be used or the precise geometry of the different ionization zones of each nebula should be known. However, the difference of  $\text{He}^+/\text{H}^+$  considering  $T_e(\text{He I})$  and  $T_e([\text{O III}])$  is expected to be small given the small dependence on temperature of the intensity ratios of recombination lines. The difference between  $T_e(\text{He I})$  and  $T_e([\text{O III}])$  is important for those interested in determining the primordial helium abun-

dance, with the least possible uncertainty ( $\leq 1\%$ ). In our case, an uncertainty of the order or even somewhat larger than 1% in the calculation of the  $\text{He}^+/\text{H}^+$  ratio is acceptable, even more taking into account that statistically those uncertainties will not be reflected in the determination of a gradient based on data of several objects and whose main source of uncertainty is not  $\text{He}^+/\text{H}^+$  but the  $\text{He}^0/\text{H}^+$  ratio. Nevertheless, we have explored the effects that  $T_e$  and optical depth effects of the metastable  $2^3S$  level –  $\tau(2^3S)$  but parametrized by  $\tau(3889)$  – would have on the  $\text{He}^+/\text{H}^+$  ratios.

Figure 2 presents the comparison between the  $\text{He}^+/\text{H}^+$  ratios obtained from the method followed in this work and those obtained using `Helio14` with the list of lines presented in Table A2 and  $T_e(\text{O II}+\text{O III})$ , derived following Peimbert et al. (2002).  $T_e(\text{O II}+\text{O III})$  takes into account the emission of He I in the low ionization zone. `Helio14` code is an updated version of `Helio10` presented by Peimbert et al.

(2012). The code uses the effective recombination coefficients of Storey & Hummer (1995) for H I, and Porter et al. (2007) for He I, the collisional contribution of He I lines calculated by Sawey & Berrington (1993) and the optical depth effects in the triplets estimated by Kingdon & Ferland (1995). `Helio14` calculates the most likely values for  $n_e(\text{He I})$ ,  $\tau(2^3S)$  and the  $\text{He}^+/\text{H}^+$  ratio from the theoretical  $\text{He I}/\text{H}\beta$  ratios using as input a set of parameters, atomic data, and up to 20  $\text{He I}/\text{H}\beta$  line intensity ratios along with their uncertainties. Then, it compares the observed ratios to the theoretical ones minimising  $\chi^2$ :

$$\chi^2 = \sum_{\lambda} \frac{\left\{ \left[ \frac{I(\lambda)}{I(\text{H}\beta)} \right]_{\text{obs}} - \left[ \frac{I(\lambda)}{I(\text{H}\beta)} \right]_{\text{theo}} \right\}^2}{\sigma_I(\lambda)^2}. \quad (1)$$

Where  $\sigma_I(\lambda)$  is the uncertainty in the intensity of  $\lambda$ . The comparison of Figure 2 shows that all the objects are entirely consistent with the 1:1 relation. The nebulae with the largest deviations with respect the 1:1 line are RCW 52, Sh 2-209 and Sh 2-308, although the values agree with such relation within the uncertainties. These three objects are among the ones with fewer He I lines in their spectra: 4, 4 and 2, respectively, so the determination of the abundance of He I is very sensitive to the variations of the fitted parameters in the minimisation of  $\chi^2$ . `Helio14` determines the available parameter space within  $\chi_{\text{min}}^2 < \chi^2 < \chi_{\text{min}}^2 + 1$  to estimate the  $1\sigma$  error bars. In any case, from these 3 objects, just RWC 52 was taken into account in the determination of radial He I gradients. The rest are ring nebula associated Wolf-Rayet stars and they present an overabundance of helium. This is discussed in greater detail in §5. The general deviation between the values of  $\text{He}^+/\text{H}^+$  ratios obtained with `Helio14` and those obtained following the procedure described in this section is less than 0.008 dex even including the 3 objects showing the largest differences.

From all the spectra in our sample, we have deconvolved He I  $\lambda 3889.64$  from H I  $\lambda 3889.05$  by multiple Gaussian fitting in NGC 3576 and Sh 2-311. Among all the spectra, only Sh 2-152, NGC 3576, NGC 7635-A4, M16, M17, M20 and M42 have measurements of the intensity ratio of He I  $\lambda 3889.64$  or the blend of He I  $\lambda 3889.64$  and H I  $\lambda 3889.05$  with  $\text{H}\beta$  with uncertainties smaller than 3%. In these last cases, we study the possible effect of  $\tau(3889)$  on the determination of the  $\text{He}^+/\text{H}^+$  ratios. A small uncertainty in the measurement of He I  $\lambda 3889.64$  is indispensable to avoid spreading uncontrolled errors in  $\tau(3889)$  and consequently in the abundance of  $\text{He}^+/\text{H}^+$ .

In the nebulae where both lines cannot be deblended with multiple Gaussian fitting, the contribution of He I  $\lambda 3889.64$  to the total intensity was obtained after subtracting its theoretical ratio to H I  $\lambda 3889.05$  based on the work by Brocklehurst (1971). In Figure 3 we compare the values of the  $\text{He}^+/\text{H}^+$  ratios for Sh 2-152, NGC 3576, NGC 7635-A4, M16, M17, M20 and M42 using `Helio14` with the same input parameters as in Figure 2 but taking into account  $\tau(3889)$  and the results we obtain with our methodology. The general dispersion is smaller than 0.007 dex. From this comparison, we can conclude that our results can be considered virtually independent of the effects of  $\tau(2^3S)$ . In fact, this is minimised by averaging  $\text{He}^+/\text{H}^+$  ratios from a large

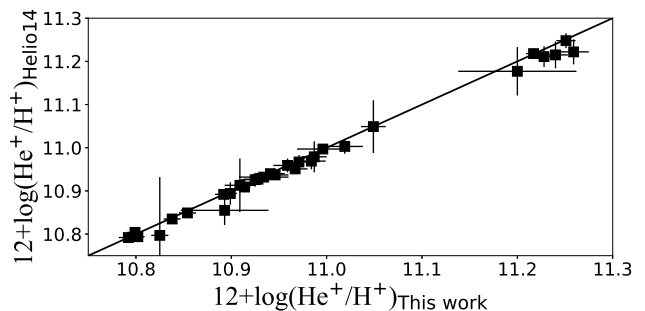


**Figure 2.** General comparison of the average  $\text{He}^+/\text{H}^+$  ratios obtained for the sample objects using our methodology described in the text and using the `Helio14` code (Peimbert et al. 2012). The continuous line indicates the 1:1 relation.

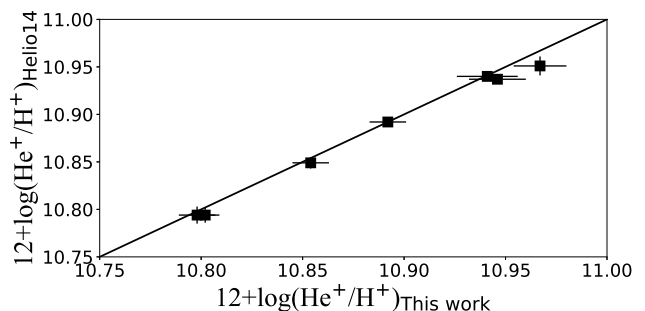


**Figure 3.** Comparison between  $\text{He}^+/\text{H}^+$  determinations after estimating the effects of optical depth ( $\tau(3889)$ ) in 7 objects: Sh 2-152, NGC 3576, NGC 7635-A4, M16, M17, M20 and M42. The continuous line indicates the 1:1 relation.

number of emission lines, including several singlets, which intensities are practically independent of  $\tau(2^3S)$ .

Among the brightest He I lines,  $\lambda 4922$ ,  $\lambda 5876$  and  $\lambda 6678$  have been considered for calculating the weighted mean in more than 84% of the spectra in which they have been measured (most or all of them). Other well-behaved less intense He I lines are  $\lambda 3614$ ,  $\lambda 3965$ ,  $\lambda 4026$ ,  $\lambda 4388$  and  $\lambda 4438$ , that have been taken for calculating the mean in more than 70% of the spectra in which they have been measured. Most of these lines (6) corresponds to singlets, and only 2 to triplets ( $\lambda 4026$  and  $\lambda 5876$ ). The He I lines that have a greater tendency to provide less consistent values with respect to the average  $\text{He}^+/\text{H}^+$  ratio are:  $\lambda 4121$ ,  $\lambda 4713$ ,  $\lambda 5048$ ,  $\lambda 7281$  and  $\lambda 9464$ , that have been used in less than 50% of the objects in which they have been measured. Of these, 2 are singlets and 3 triplets. In the case of the 2 lines of red-der wavelength,  $\lambda 7281$  and  $\lambda 9464$ , their line intensity may be affected by contamination with telluric emission or absorption features. In fact, when these lines are observed with high-resolution echelle spectroscopy, the  $\text{He}^+$  abundances obtained from them are similar to those obtained from other more intense lines and they are considered to compute the average value of the  $\text{He}^+/\text{H}^+$  ratio. The He I  $\lambda 5015$  line is relatively bright but has not been considered in many spectra because it is blended with the [O III]  $\lambda 5007$  line in the OSIRIS spectra and affected by a ghost emission feature in

the UVES ones. Another bright He I line is  $\lambda 4471$ , but it is only used in 59% of the spectra. This is mainly because it provides  $\text{He}^+/\text{H}^+$  ratios lower than the mean in G2.4+1.4, NGC 6888 and NGC 7635, the objects with the largest number of spectra. The whole optical OSIRIS spectra of these objects were taken with two gratings, R1000B and R2500V. Since the He I  $\lambda 4471$  line was the closest one to the blue edge of the spectra taken with in R2500V, some deviations at the border of the flux calibration curve may be affecting the flux measurement obtained by [Esteban et al. \(2016\)](#) for this line.

### 3.3 Total He abundances

The presence of  $\text{He}^0$  inside the  $\text{H}^+$  zone may be significant in low ionization nebulae. We need to assume an ICF(He) to determine the total helium abundance from the measured  $\text{He}^+/\text{H}^+$  ratio, in the form:  $\text{He}/\text{H} = \text{ICF}(\text{He}) \cdot \text{He}^+/\text{H}^+$ . However, the estimation of the ICF(He) is a controversial issue and there is no a consensus among the different authors. Traditional ICF(He) schemes involve abundance ratios of different heavy-element ions such as  $\text{O}^+$ ,  $\text{O}^{2+}$ ,  $\text{S}^+$  or  $\text{S}^{2+}$ . For the H II regions of our sample, we have used the values of  $\text{O}^+$ ,  $\text{O}^{2+}$ ,  $\text{S}^+$  and  $\text{S}^{2+}$  abundances determined by [Arellano-Córdova et al. \(2020\)](#), who use PYNEB and the atomic data given in Table 2. In addition, we have re-calculated the  $\text{N}^+$  abundances of the WR ring nebulae using the same methodology, their N abundances will be discussed in §5. The line intensities used to derive the heavy-element ionic abundances have been [O II]  $\lambda\lambda 3726, 3729$ , [O II]  $\lambda\lambda 4959, 5007$ , [S II]  $\lambda\lambda 6717, 6731$ , [S III]  $\lambda 6312$  (we used also [S III]  $\lambda\lambda 9069, 9035$  in several objects) and [N II]  $\lambda\lambda 6548, 6583$ . Their reddening-corrected values have been taken from the set of source papers. [Arellano-Córdova et al. \(2020\)](#) use  $T_e([\text{N II}])$  as representative of the  $\text{O}^+$ ,  $\text{S}^+$  and  $\text{N}^+$  emitting regions and  $T_e([\text{O III}])$  as representative of the  $\text{O}^{++}$  zone. Following the recommendation of [Domínguez-Guzmán et al. \(2019\)](#), [Arellano-Córdova et al. \(2020\)](#) adopt the mean value of  $T_e([\text{N II}])$  and  $T_e([\text{O III}])$  to calculate the  $\text{S}^{++}$  abundance. In the sake of homogeneity and as we did for determining the physical conditions, we used the same methodology and atomic data as [Arellano-Córdova et al. \(2020\)](#) for deriving the  $\text{O}^+$ ,  $\text{O}^{2+}$ ,  $\text{S}^+$ ,  $\text{S}^{2+}$  or  $\text{N}^+$  abundances for the ring nebulae. The heavy-element ionic abundances determined for each spectrum and object are included in Table 3.

Photoionization models (e.g. [Stasińska & Schaerer 1997](#)) predict that helium is completely ionized inside the  $\text{H}^+$  zone when the exciting star is hotter than about 39 000K (earlier than O6.5V), independently of the ionization parameter. Most of the ionizing stars of our sample are ionized by stars that should be colder, so one would expect a certain amount of  $\text{He}^0$  in most of our nebulae. On the other hand, observations in different directions inside H II regions carried out by [Deharveng et al. \(2000\)](#) show that even an H II region excited by a star of spectral type earlier than O6.5 can contain a significant amount of  $\text{He}^0$ . We have used different ICF(He) schemes because, as we have said before, there is not a standard method to correct for the fraction of  $\text{He}^0$ , although all schemes consider that the higher the ionization degree the higher the  $\text{He}^+/\text{He}$  ratio of the nebulae. ICF(He) schemes usually consider the similarity between the ionization potential of  $\text{He}^0$  (24.59 eV) and those of  $\text{S}^+$

(23.33 eV) and/or  $\text{O}^+$  (34.97 eV) assuming that the relation  $\text{O}^+/\text{O} > \text{He}^0/\text{He} > \text{S}^+/\text{S}$  should be applicable but using different parameters proportional to the ionization degree of the nebula. One of the first ICF(He) schemes was proposed by [Peimbert & Torres-Peimbert \(1977\)](#) in their work on the chemical composition of the Orion Nebula that uses a linear combination of  $\text{O}^+/\text{O}$  and  $\text{S}^+/\text{S}$  ratios,

$$\text{ICF}(\text{He})_{\text{PTP77}} = \left[ 1 - \gamma \cdot \frac{\text{O}^+}{\text{O}} - (1 - \gamma) \cdot \frac{\text{S}^+}{\text{S}} \right]^{-1}. \quad (2)$$

The value of  $\gamma$  depends on the density distribution ([Peimbert et al. 1974](#)). It can be determined when spectra at different positions covering different ionization conditions are available for the nebula, but this is not the case for most of our sample objects. The only objects with several slit positions are all ring nebulae and bubbles, that are better represented by relatively thin ionized shells rather than typical StrÅumgren spheres and, therefore, that method for estimating the parameter  $\gamma$  may not be appropriate. [Peimbert & Torres-Peimbert \(1977\)](#) estimated  $\gamma = 0.35$  in the case of the Orion Nebula and [Peimbert et al. \(1978\)](#) found  $\gamma = 0.20$  for  $\eta$  Carina nebula. Those last authors assume the same value of 0.20 for other H II regions with  $n_e$  values similar to that of  $\eta$  Carina nebula (300-1000  $\text{cm}^{-3}$ ). [Lequeux et al. \(1979\)](#) use equation 2 for determining the He abundance for a sample of metal-poor H II galaxies with  $n_e$  in the 10-100  $\text{cm}^{-3}$  range using  $\gamma = 0.15$ . In our case, following the prescriptions given in the cited works, we have used equation 2 using values of  $\gamma$  interpolating between 0.15 to 0.35 as a function of the  $n_e$  of the nebulae.

Other ICF(He) schemes only use  $\text{O}^+/\text{O}$  or  $\text{S}^+/\text{S}$  ratios as indicators of the ionization degree of the nebulae. [Kunth & Sargent \(1983\)](#), in their study of a sample of metal-poor galaxies, proposed an ICF(He) dependent on the  $\text{O}^+/\text{O}$  ratio deduced from [Peimbert et al. \(1974\)](#) empirical models,

$$\text{ICF}(\text{He})_{\text{KS83}} = \left[ 1 - 0.25 \cdot \frac{\text{O}^+}{\text{O}} \right]^{-1}. \quad (3)$$

[Peimbert et al. \(1992\)](#) presented a detailed spectroscopical study of the highly-ionized Galactic H II region M17 and propose an ICF(He) parameterized only by the  $\text{S}^+/\text{S}$  ionization fraction. [Zhang & Liu \(2003\)](#) use a very similar scheme in their study of the relatively low excitation planetary nebula M 2-24 but depending on the  $\text{S}^+/\text{S}^{2+}$  ratio, which – in contrast to  $\text{S}^+/\text{S}$  – is a parameter that can be obtained directly from optical spectra:

$$\text{ICF}(\text{He})_{\text{ZL03}} = 1 + \frac{\text{S}^+}{\text{S}^{2+}}. \quad (4)$$

[Delgado-Inglada et al. \(2014\)](#) do not recommend the use of traditional ICF(He) schemes – as those given in equations 3 and 4 – because the  $\text{He}^0/\text{He}^+$  ratio is more dependent on the effective temperature of the ionizing source, whereas heavy-element abundance ratios depend essentially on the ionization parameter. [Vilchez \(1989\)](#) proposed an ICF(He) scheme based on the radiation softness parameter defined as  $\eta = (\text{O}^+/\text{S}^+) \cdot (\text{S}^{2+}/\text{O}^{2+})$  ([Vilchez & Pagel 1988](#)), which is sensitive to the effective temperature of the ionizing source and a good indicator of the ionization structure of the nebula. [Vilchez \(1989\)](#) and [Pagel et al. \(1992\)](#) pointed out that for  $\log(\eta) < 0.9$  the amount of  $\text{He}^0$  inside the  $\text{H}^+$  zone is negligible for a large variety of models, but becomes very

**Table 4.** Total He abundances<sup>a</sup> for the sample objects using different ICF schemes.

Object	PTP77	ICF(He) scheme <sup>b</sup>		B09
		ZL03	KS83	
G2.4+1.4		11.038 ± 0.017 <sup>c</sup>		
M8	10.963 ± 0.038	10.897 ± 0.016	10.927 ± 0.032	11.098 ± 0.093
M16	11.094 ± 0.066	11.031 ± 0.033	10.985 ± 0.034	10.982 ± 0.106
M17	10.994 ± 0.020	10.984 ± 0.016	10.987 ± 0.018	10.987 ± 0.052
M20	11.043 ± 0.055	10.968 ± 0.028	10.957 ± 0.033	11.095 ± 0.125
M42	10.981 ± 0.031	10.964 ± 0.022	10.964 ± 0.022	10.953 ± 0.054
NGC 2579	10.998 ± 0.046	10.972 ± 0.033	10.978 ± 0.040	10.976 ± 0.095
NGC 3576	10.995 ± 0.028	10.975 ± 0.021	10.977 ± 0.023	10.964 ± 0.054
NGC 3603	11.008 ± 0.032	11.002 ± 0.029	11.004 ± 0.030	11.010 ± 0.082
NGC 6888		11.244 ± 0.011 <sup>c</sup>		
NGC 7635	11.051 ± 0.030	11.031 ± 0.034	11.041 ± 0.034	11.087 ± 0.057
RCW 52	10.960 ± 0.162	10.903 ± 0.070	10.921 ± 0.134	11.144 ± 0.514
RCW 58	11.279 ± 0.046	11.242 ± 0.019	11.284 ± 0.051	11.503 ± 0.306
Sh 2-83	10.916 ± 0.015	10.921 ± 0.014	10.908 ± 0.010	10.997 ± 0.163
Sh 2-100	11.009 ± 0.024	11.000 ± 0.020	11.003 ± 0.021	11.003 ± 0.071
Sh 2-127	10.944 ± 0.045	10.863 ± 0.022	10.906 ± 0.034	10.967 ± 0.195
Sh 2-128	11.004 ± 0.040	10.976 ± 0.029	10.976 ± 0.029	10.957 ± 0.083
Sh 2-152	10.920 ± 0.028	10.840 ± 0.014	10.906 ± 0.024	11.327 ± 0.090
Sh 2-209	10.979 ± 0.154	10.960 ± 0.104	10.936 ± 0.100	10.896 ± 0.081
Sh 2-212	11.128 ± 0.155	11.085 ± 0.077	11.101 ± 0.128	11.197 ± 0.482
Sh 2-288	10.928 ± 0.090	10.864 ± 0.050	10.880 ± 0.052	10.998 ± 0.289
Sh 2-298	11.252 ± 0.138	11.260 ± 0.062	11.032 ± 0.040	11.136 ± 0.134
Sh 2-308	11.222 ± 0.094	11.226 ± 0.086	11.212 ± 0.080	11.264 ± 0.469
Sh 2-311	11.080 ± 0.046	11.037 ± 0.021	11.002 ± 0.030	10.992 ± 0.070

<sup>a</sup> In units of  $12 + \log(\text{He}/\text{H})$ .

<sup>b</sup> PTP77: Peimbert & Torres-Peimbert (1977); ZL03: Zhang & Liu (2003); KS83: Kunth & Sargent (1983); B09: Bresolin et al. (2009).

<sup>c</sup>  $\text{He}/\text{H} = \text{He}^+/\text{H}^+ + \text{He}^{2+}/\text{H}^+$  for this object. No ICF(He) applied.

model dependent for  $\log(\eta) > 1$ . Izotov et al. (1994) and Bresolin et al. (2009) have obtained approximate analytical expressions of ICF(He) as a function of  $\eta$  parameter based on photoionization models. In our case, we have used the relation given by Bresolin et al. (2009) in their study of H II regions in the spiral galaxy NGC 300 and based on the predictions of photoionization models by Stasińska et al. (2001),

$$\text{ICF}(\text{He})_{\text{B09}} = 1.585 + \log(\eta) \cdot [1.642 \cdot \log(\eta) - 1.948]. \quad (5)$$

In the case of the ring nebulae for which we have spectra at several slit positions and, therefore, several independent determinations of the He abundance, we have selected the representative He/H ratio of the nebula as a whole attending to different considerations in each object. In the case of G2.4+1.4, we only considered the spectra of zone A2, which has the highest signal-to-noise ratio and was observed with higher spectral resolution (MagE echelle spectrograph). In the case of NGC 6888, we take the weighted mean value of zones A3, A4, A5 and A6, which are located in the main body of the ionized nebula. Zones A1 and A2 correspond to high-ionization narrow peripheral arcs showing very high values of  $T_e$  and may be contaminated by shock excitation (see Esteban et al. 2016). For NGC 7635 we have taken the weighted mean value of zones A2, A3, A5 and A6, which correspond to the relatively highly-ionized gas of the expanding bubble. Zone A1 of NGC 7635 corresponds to one of the brightest knots of Sh 2-162, a large H II region that encompasses the ring nebula NGC 7635. Sh 2-162 is ionized by the same O-type star but shows a lower ionization degree. Zone A4 covers the brightest of a group of several high-density

cometary knots just at the southwest of the ionizing star that show rather higher densities and quite lower ionization degrees.

The WR ring nebulae G2.4+1.4 and NGC 6888 show He II lines in their spectra (Esteban et al. 2016). G2.4+1.4 is a high ionization degree object ionized by a very hot WO2 star and the He II  $\lambda 4686$  line is very bright. We have determined the  $\text{He}^{2+}$  abundance using PYNEB,  $T_e([\text{O III}])$  and the effective recombination coefficient calculated by Storey & Hummer (1995), obtaining  $12 + \log(\text{He}^{2+}/\text{H}^+) = 10.45 \pm 0.02$  for the zone A2 of G2.4+1.4. In the case on NGC 6888 the  $\text{He}^{2+}$  abundances we determine for the different zones is very much lower, with values ranging from 8.14 to 8.51, which are clearly negligible in comparison to the  $\text{He}^+/\text{H}^+$  ratio determined in this object. We did not use an ICF(He) for G2.4+1.4 and NGC 6888 and their total He abundance was simply  $\text{He}^+/\text{H}^+ + \text{He}^{2+}/\text{H}^+$ .

In Table 4 we show the He/H ratios obtained for each nebulae using the different ICF(He) schemes considered. In the case of the ICF(He)<sub>PTP77</sub>, there is an explicit dependence of the S/H ratio, which has been derived from the sum of the  $\text{S}^+$  and  $\text{S}^{2+}$  abundances given in Table 3 and an appropriate ICF(S) using the relations:

$$\frac{\text{S}}{\text{H}} = \text{ICF}(\text{S}) \cdot \left[ \frac{\text{S}^+}{\text{H}^+} + \frac{\text{S}^{2+}}{\text{H}^+} \right], \quad (6)$$

where

$$\text{ICF}(\text{S}) = \left[ 1 - \left( 1 - \frac{\text{O}^+}{\text{O}} \right)^3 \right]^{-1/3}, \quad (7)$$

which was proposed by Stasińska (1978). The uncertainty of the total He abundance has been determined propagating the errors of the  $\text{He}^+/\text{H}^+$  ratio and that of the  $\text{ICF}(\text{He})$  – and  $\text{ICF}(\text{S})$  – used, which comes from the derivation of each equation of the ICF and the quoted errors of the ionic abundances given in Table 3.

#### 4 THE GALACTIC RADIAL ABUNDANCE GRADIENT OF HELIUM

In Fig. 4 we show the radial distribution of the He abundances of the H II regions of our sample – a total of 19 objects – using the different  $\text{ICF}(\text{He})$  schemes introduced in equations 2 to 5. We have also included the ring nebulae around O-type objects in this group because they do not contain chemically enriched material from the central star (see Esteban et al. 2016). In these diagrams we have separated the nebulae in two groups, those with  $\log(\eta) < 0.9$  – which are expected to contain a small fraction of  $\text{He}^0$  – represented with full black squares and the rest of them (grey empty squares). This separation is made in order to explore the radial distribution of the He abundances minimizing the effect of the  $\text{ICF}(\text{He})$  and maintaining a reasonable number of objects distributed along a significant part of the Galactic disc. The least-squares linear fits to the objects with  $\log(\eta) < 0.9$  (solid lines) and to all the objects included in each panel (dotted lines) are also included in each panel of Fig. 4. The parameters of the fits along with their associated uncertainties are shown in Table 5. The uncertainties of the slope and intercept of the linear fits are computed through Monte Carlo simulations. We generate 10,000 random values of  $R_G$  and the He/H ratios for each observational point assuming a Gaussian distribution with a sigma equal to the uncertainty of each quantity. We performed a least-squares linear fit to each of these random distributions. It is important to remark that the uncertainty of  $R_G$  has been considered in the fittings, which is not usually taken into account in most works except, for example, in Esteban et al. (2017) or Esteban & García-Rojas (2018). The uncertainties associated to the slope and intercept correspond to the standard deviation of the values of these two quantities obtained from the fits. From the radial gradients represented in Fig. 4 and their parameters collected in Table 5, we can see that although the uncertainties of the slopes are larger than the slope values in most cases, they show pretty similar values in all cases, especially when only the objects with  $\log(\eta) < 0.9$  are considered. More importantly, the gradients are always negative independently on the  $\text{ICF}(\text{He})$  scheme used.

In Fig. 5 we show the radial distribution and the least-squares linear fit of the He abundances of the H II regions with  $\log(\eta) < 0.9$  assuming no  $\text{ICF}(\text{He})$ , i.e.  $\text{He}/\text{H} = \text{He}^+/\text{H}^+$ . Each data point is represented with a colour proportional to its  $\log(\eta)$ , and the diagram indicates that the value of the  $\eta$  parameter does not seem to determine the behaviour of the gradient. In fact, the objects with the lowest values of  $\log(\eta)$  (i.e. those with the lowest expected fraction of  $\text{He}^0$ ) are precisely those located at larger  $R_G$  showing lower  $\text{He}^+/\text{H}^+$  ratios. In Fig. 6, we can compare the least-squares linear fits of the He abundances obtained for the H II regions with  $\log(\eta) < 0.9$  assuming different  $\text{ICF}(\text{He})$  schemes or no  $\text{ICF}(\text{He})$ . In the figure we can see that the slopes are rather similar in

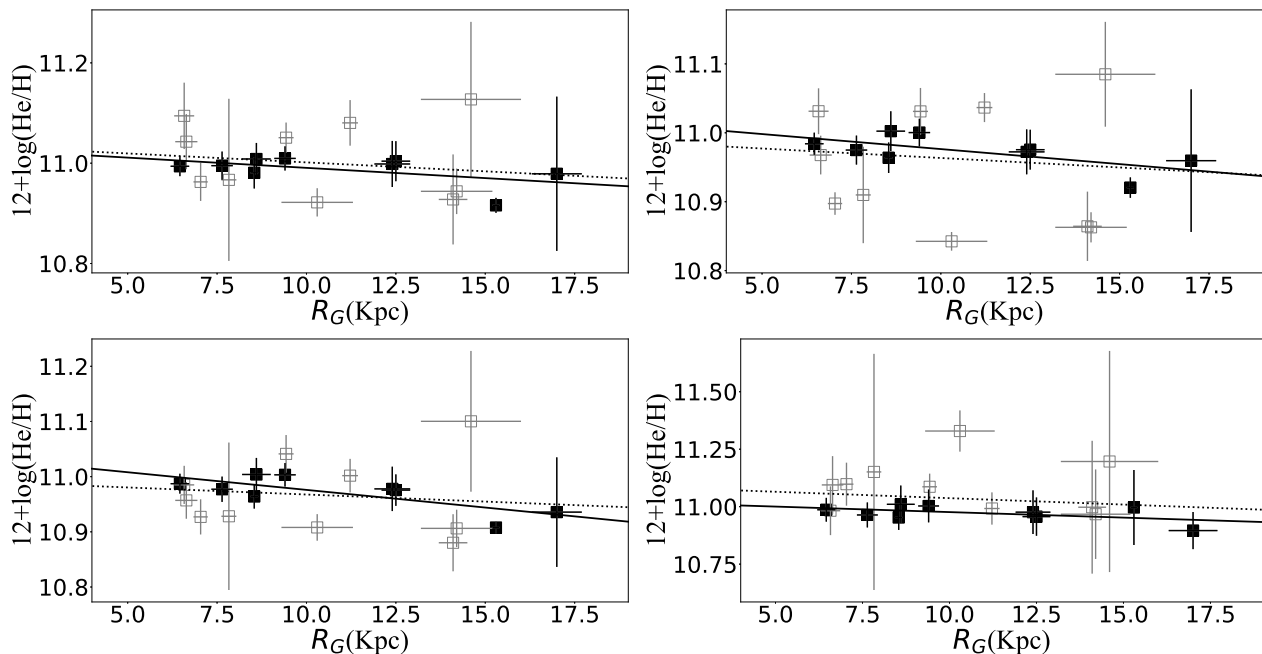
all cases, going from  $-0.0078$  to  $-0.0044$  dex  $\text{kpc}^{-1}$ , with a dispersion of values smaller than the typical uncertainty of each individual determination of the slope. The differences are larger when we compare the values of the He/H given by each fit for a given  $R_G$ . The no- $\text{ICF}(\text{He})$  case gives the lowest values of the He/H ratio – as expected – and the  $\text{ICF}(\text{He})$  by Peimbert & Torres-Peimbert (1977) gives the largest ones. It is interesting to note that the other  $\text{ICF}(\text{He})$  schemes give He/H values that differ less than 0.02 dex. It is remarkable that the ICF scheme from Bresolin et al. (2009) is the most sensitive to the propagation of the errors. Its use requires very precise determinations of  $\text{O}^+$ ,  $\text{S}^+$ ,  $\text{O}^{2+}$  and  $\text{S}^{2+}$ .

The presence of abundance gradients of heavy elements – such as O, N, Ne, S, Ar or Cl – along the disc of the galaxy is a well established fact from the observational point of view (e.g. Shaver et al. 1983; Deharveng et al. 2000; Rudolph et al. 2006; Balser et al. 2011; Esteban & García-Rojas 2018). However, although theoretical models predict its existence, this has not been the case for He. Very recent cosmological chemodynamical simulations for galaxy formation and evolution predict negative radial gradients of He/H due to the inside-out growth of galaxy discs as a function of time (Vincenzo et al. 2019). Previous chemical evolution models of the Milky Way disc by Matteucci & Chiappini (1999) and Chiappini et al. (2002) predicted He/H gradients with slopes between  $-0.0085$  and  $-0.002$  dex  $\text{kpc}^{-1}$  in the  $R_G$  range from 4 to 18 kpc. Kubryk et al. (2015) obtain a similar range of values (from about  $-0.007$  to  $-0.003$  dex  $\text{kpc}^{-1}$ ) from models including radial motions of gas and stars in the Milky Way disc and different sets of stellar yields. These values are pretty consistent with our results given in Table 5. From the observational point of view, the evidence of a Galactic radial gradient of the He/H has been elusive. Peimbert et al. (1978) found a negative gradient of  $-0.02 \pm 0.01$  dex  $\text{kpc}^{-1}$  from the analysis of the abundance obtained from 3 He I lines in a small sample of 5 Galactic H II regions. Talent & Dufour (1979) obtain a marginal evidence of a negative gradient,  $-0.008 \pm 0.008$  dex  $\text{kpc}^{-1}$  for a larger sample of objects based solely on the intensity of He I  $\lambda 5876$  and  $\lambda 6678$  lines. Other works as Hawley (1978), Shaver et al. (1983), Deharveng et al. (2000) or Fernández-Martín et al. (2017) find a flat He abundance distribution along the Galactic disc from observations of a limited number of He I lines in samples with different number of objects. In their work, Fernández-Martín et al. (2017) include some of the H II regions of our sample (Sh2-83, Sh2-212 and NGC 7635), whose data are based on other spectroscopic observations. The  $\text{He}^+/\text{H}^+$  ratios per line shown in their Table A.2. are consistent with our results, although there are slight differences attributable to the different recombination coefficients used. However, the methodology followed by Fernández-Martín et al. (2017) to adopt a final  $\text{He}^+/\text{H}^+$  value differs from ours, among other things, by the use of fewer He I lines and the inclusion of He I  $\lambda 7065$ . Although their sample includes spectra of some Galactic H II regions not considered in the present paper, we decided not to include them for the sake of having a group of nebulae with a homogeneous data reduction process; furthermore, the  $R_G$  of those objects are well covered by the H II regions of our sample.

Other determinations of the radial He/H gradient in the Milky Way come from the analysis of the emission-line spec-

**Table 5.** Radial He/H gradients using different combinations of H II regions and ICF schemes.

ICF(He)	All H II regions		Only with $\log(\eta) < 0.9$	
	Slope (dex kpc <sup>-1</sup> )	Intercept	Slope (dex kpc <sup>-1</sup> )	Intercept
PTP77	$-0.0036 \pm 0.0069$	$11.04 \pm 0.07$	$-0.0046 \pm 0.0091$	$11.04 \pm 0.08$
ZL03	$-0.0028 \pm 0.0043$	$10.99 \pm 0.04$	$-0.0044 \pm 0.0062$	$11.02 \pm 0.06$
KS83	$-0.0025 \pm 0.0049$	$10.99 \pm 0.05$	$-0.0067 \pm 0.0060$	$11.04 \pm 0.06$
B09	$-0.006 \pm 0.015$	$11.09 \pm 0.07$	$-0.0051 \pm 0.0077$	$11.09 \pm 0.15$
No ICF(He)	--	--	$-0.0078 \pm 0.0029$	$11.03 \pm 0.03$


**Figure 4.** Radial distribution of the He abundances of the H II regions of our sample using different ICF(He) schemes. Upper left: using the ICF(He) proposed by Peimbert & Torres-Peimbert (1977, PTP77); upper right: ICF(He) by Zhang & Liu (2003, ZL03); lower left: ICF(He) by Kunth & Sargent (1983, KS83); lower right: ICF(He) by Bresolin et al. (2009, B09). Black full squares indicate H II regions with  $\log(\eta) < 0.9$  and grey empty squares indicate H II regions with  $\log(\eta) \geq 0.9$ . Solid lines represent the least-squares linear fits only to the objects with  $\log(\eta) < 0.9$  and dot lines represent the linear least-squares fits to all the objects included in each panel.

tra of Planetary Nebulae (PNe). Early works such as those by D’Odorico et al. (1976), Peimbert & Serrano (1980) or Faúndez-Abans & Maciel (1987) found slopes between  $-0.03$  and  $-0.02$  dex kpc<sup>-1</sup>, while others reported negligible gradients (e.g. Pasquali & Perinotto 1993). At any rate, PNe are not confident probes of the abundances of the ISM because they are composed of stellar ejecta material and can be contaminated by the products of nucleosynthesis. Trying to alleviate this drawback, Maciel (2001) introduced corrections to the measured He abundance owing to the contamination from the progenitor star obtaining an essentially flat radial He/H gradient for a large sample of PNe.

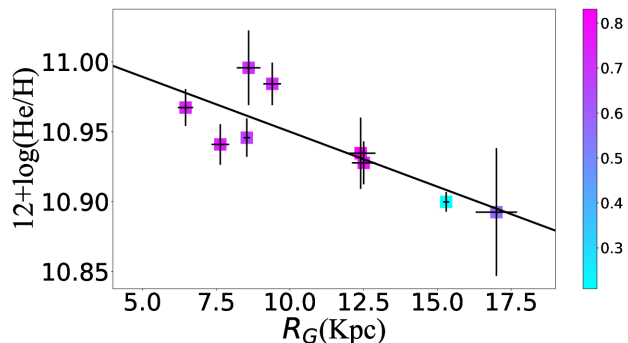
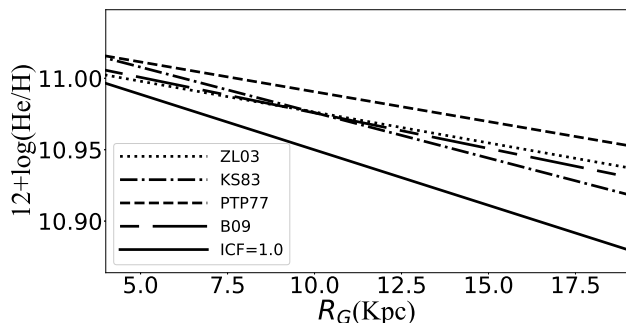
## 5 ABUNDANCE DEVIATIONS IN WR RING NEBULAE

Ring nebulae are bubbles of gas swept-up by the mechanical action of the mass loss episodes experienced by their massive stellar progenitors. They are rather common around Wolf-Rayet (WR) stars and luminous blue variables (LBVs).

There have been several spectroscopical works devoted to study the chemical composition of the ionized gas contained in ring nebulae around Galactic WR stars (e.g. Kwitter 1984; Esteban et al. 1992, 2016; Stock et al. 2011). Those works have found that some ring nebulae (NGC 6888, RCW 58, Sh 2-308 and M 1-67) show clear chemical enrichment patterns, in general they are He and N enriched and some of them show some O deficiency, indicating that they are composed by ejecta material that has suffered contamination by the CNO cycle. Esteban & Vilchez (1992) and Esteban et al. (1992) compared the abundance pattern of Galactic ejecta ring nebulae with the surface abundances predicted by evolutionary models of massive stars, finding that the He, N and O abundances of the nebulae are consistent with the expected surface composition of stars with initial masses between 25 and 40  $M_{\odot}$  at the red supergiant (RSG) phase, prior to the onset of the WR stage. Later studies by Mesa-Delgado et al. (2014) and Esteban et al. (2016) using stellar evolution models by Ekström et al. (2012) and Georgy et al. (2012) confirmed that non-rotational models of stars of initial masses between 25 and 40  $M_{\odot}$  seem to

**Table 6.** He, O and N abundance deviations with respect to abundance gradients in WR ring nebulae.

Object	12+log(He/H)	$\Delta(\text{He}/\text{H})$	12+log(O/H)	$\Delta(\text{O}/\text{H})$	12+log(N/H)	$\Delta(\text{N}/\text{H})$
G2.4+1.4	11.04 $\pm$ 0.02	+0.04 $\pm$ 0.09	8.48 $\pm$ 0.25	-0.09 $\pm$ 0.34	7.98 $\pm$ 0.23	+0.10 $\pm$ 0.27
NGC 6888	11.24 $\pm$ 0.01	+0.25 $\pm$ 0.11	8.14 $\pm$ 0.19	-0.33 $\pm$ 0.24	8.41 $\pm$ 0.30	+0.67 $\pm$ 0.36
RCW 58	11.23 $\pm$ 0.02	+0.24 $\pm$ 0.10	8.60 $\pm$ 0.16	+0.11 $\pm$ 0.20	8.67 $\pm$ 0.18	+0.91 $\pm$ 0.23
Sh 2-298	11.08 $\pm$ 0.09	+0.12 $\pm$ 0.15	8.43 $\pm$ 0.06	+0.10 $\pm$ 0.15	7.60 $\pm$ 0.13	+0.07 $\pm$ 0.20
Sh 2-308	11.22 $\pm$ 0.01	+0.24 $\pm$ 0.12	7.89 $\pm$ 0.23	-0.51 $\pm$ 0.28	8.05:	+0.41:

**Figure 5.** Radial distribution of the He abundances of the H II regions with  $\log(\eta) < 0.9$  assuming no ICF(He) (i.e.  $\text{He}/\text{H} = \text{He}^+/\text{H}^+$ ). The colour of the squares indicates the value of  $\log(\eta)$  of each object. The solid lines represent the least-squares linear fits to the data.**Figure 6.** Comparison of the least-squares linear fits of the He abundances obtained for the H II regions with  $\log(\eta) < 0.9$  assuming different ICF(He) schemes or no ICF(He). Solid line: no ICF(He); dash line: ICF(He) by Peimbert & Torres-Peimbert (1977, PTP77); dot line: ICF(He) by Zhang & Liu (2003, ZL03); dash dot line: ICF(He) by Kunth & Sargent (1983, KS83); long-dash dash line: ICF(He) by Bresolin et al. (2009, B09).

reproduce the abundance patterns in most of the ejecta nebulae, being this range wider in the case of Sh 2-308, from 25 to 50  $M_{\odot}$ . Only rotational models of 25  $M_{\odot}$  show agreement with the data for NGC 6888, RCW 58 and Sh 2-308.

The availability of new Gaia distances, the results of this paper and the recent reassessment of the Galactic radial gradients of O/H and N/H by Esteban & García-Rojas (2018), allow us to perform a better estimate of the chemical enrichment pattern in He, N and O of the WR ring nebulae observed by our group (Esteban et al. 2016). In Table 6 we give the total He/H, O/H and N/H ratios and the difference with the values expected from the radial abundance

gradients for the sample of WR ring nebulae included in Table 1. The He abundances of each object have been taken from Table 4. In the case of RCW 58, Sh 2-298 and Sh 2-308, we have considered the mean and standard deviation of the 4 values obtained using the different ICF(He) schemes. The O abundances have been calculated simply adding the  $\text{O}^+/\text{H}^+$  and  $\text{O}^{2+}/\text{H}^+$  ratios given in Table 3, except in the case of G2.4+1.4, the only object where we find a substantial amount of  $\text{He}^{2+}/\text{H}^+$ . In this case, we have considered the ICF(O) proposed by Delgado-Inglada et al. (2014) for determining the O/H ratio. The N/H ratio has been calculated using the  $\text{N}^+$  abundance given in Table 3 and the classical ICF(N) by Peimbert & Costero (1969), that assumes  $\text{N}/\text{O} = \text{N}^+/\text{O}^+$ .

In Table 6 we can see that G2.4+1.4 and Sh 2-298 do not show He/H, O/H and N/H ratios significantly larger than the expected values from the radial gradients considering the abundance uncertainties. NGC 6888, RCW 58 and Sh 2-308 show clear overabundances of He/H and N/H, although the errors in the last nebula are rather large due to its highly uncertain  $\text{O}^+/\text{H}^+$  ratio. The overabundance of He/H is very similar in the three objects, of about  $+0.24 \pm 0.11$  dex. Only NGC 6888 and Sh 2-308 show some possible oxygen deficiency, a result that would indicate that ON-cycle of the CNO burning has been more effective than CN-cycle in the interior of the massive progenitor stars of the nebulae (Esteban et al. 2016). These results confirm that only NGC 6888, RCW 58 and Sh 2-308 should be considered ejecta nebulae.

## 6 CONCLUSIONS

We determine the radial abundance gradient of helium of the Milky Way from published spectra of H II regions. The data set is the largest collection of deep spectra of Galactic H II regions available. We also include data of similar quality for several ring nebulae surrounding massive O and WR stars. The total number of nebulae included in the sample is 24. We have revised the Galactocentric distances of the objects,  $R_G$ , considering Gaia DR2 parallaxes and previous kinematic and spectroscopical determinations. We have determined the physical conditions  $-n_e$  and  $T_e$  – and the ionic abundance of  $\text{He}^+$  and other selected ions in a homogeneous way and using the most recent atomic data sets. We have determined the  $\text{He}^+$  abundance using several He I recombination lines. In the case of the H II regions, we have used between 3 and 10 individual He I lines depending on the object, selecting only those well-measured lines that are not affected by line-blending, telluric contamination or important self-absorption effects. The total He abundance of the objects have been estimated using four different ICF(He)

schemes based on different ionic ratios. We have determined the Galactic radial He abundance gradient using the results of 19 objects, including H II regions and ring nebulae around O-type stars. We find that although the uncertainties of the slopes are larger than the slope values obtained using several of the four ICF(He) schemes, they show consistent values in all cases, especially when only the objects with  $\log(\eta) < 0.9$  are considered. More importantly, the gradients are always negative independently on the ICF(He) scheme used. The slope values go from  $-0.0078$  to  $-0.0044$  dex  $\text{kpc}^{-1}$ , consistent with the predictions of different chemical evolution models of the Milky Way and chemodynamical simulations of galactic discs. We have estimated the abundance deviations of He, O and N of the ring nebulae around WR stars included in our sample with respect to the radial gradients, finding that only NGC 6888, RCW 585 and Sh 2-308 can be considered ejecta nebulae. These objects show He and N overabundances. The degree of enrichment of He is very similar and about  $+0.24 \pm 0.11$  dex in the three objects. NGC 6888 and Sh 2-308 show a possible O deficiency.

#### ACKNOWLEDGEMENTS

We thank the referee Ángeles I. Díaz for a constructive report. We acknowledge support from the State Research Agency (AEI) of the Spanish Ministry of Science, Innovation and Universities (MCIU) and the European Regional Development Fund (FEDER) under grant with reference AYA2015-65205-P. JG-R acknowledges support from an Advanced Fellowship from the Severo Ochoa excellence program (SEV-2015-0548). The authors acknowledge support under grant P/308614 financed by funds transferred from the Spanish Ministry of Science, Innovation and Universities, charged to the General State Budgets and with funds transferred from the General Budgets of the Autonomous Community of the Canary Islands by the MCIU. KZA-C acknowledges support from Mexican CONACYT postdoctoral grant 364239. JEM-D thanks the Fundación Carolina for the support provided for his Master's studies. JEM-D also thanks the support of the Instituto de Astrofísica de Canarias under the Astrophysicist Resident Program and acknowledges support from the Mexican CONACyT (grant CVU 602402). This work has made use of data from the European Space Agency (ESA) mission *Gaia* (<https://www.cosmos.esa.int/gaia>), processed by the *Gaia* Data Processing and Analysis Consortium (DPAC, <https://www.cosmos.esa.int/web/gaia/dpac/consortium>). Funding for the DPAC has been provided by national institutions, in particular the institutions participating in the *Gaia* Multilateral Agreement.

#### DATA AVAILABILITY

This research is based on public data available in the references. The whole dataset can be obtained from the authors by request. All the results are available in the tables and in the appendix of this article.

#### REFERENCES

- Anderson L. D., Armentrout W. P., Johnstone B. M., Bania T. M., Balser D. S., Wenger T. V., Cunningham V., 2015, *ApJS*, **221**, 26
- Arellano-Córdova K. Z., Esteban C., García-Rojas J., Méndez-Delgado J. E., 2020, arXiv e-prints, p. [arXiv:2005.11372](https://arxiv.org/abs/2005.11372)
- Avedisova V. S., Kondratenko G. I., 1984, *Nauchnye Informatsii*, **56**, 59
- Aver E., Olive K. A., Skillman E. D., 2015, *J. Cosmology Astropart. Phys.*, **2015**, 011
- Bailer-Jones C. A. L., Rybizki J., Foesneau M., Mantelet G., Andrae R., 2018, *AJ*, **156**, 58
- Balser D. S., Rood R. T., Bania T. M., Anderson L. D., 2011, *ApJ*, **738**, 27
- Benjamin R. A., Skillman E. D., Smits D. P., 2002, *ApJ*, **569**, 288
- Binder B. A., Povich M. S., 2018, *ApJ*, **864**, 136
- Bland-Hawthorn J., Gerhard O., 2016, *ARA&A*, **54**, 529
- Bohigas J., Tapia M., 2003, *AJ*, **126**, 1861
- Bresolin F., Gieren W., Kudritzki R.-P., Pietrzyński G., Urbaneja M. A., Carraro G., 2009, *ApJ*, **700**, 309
- Brocklehurst M., 1971, *MNRAS*, **153**, 471
- Caplan J., Deharveng L., Peña M., Costero R., Blondel C., 2000, *MNRAS*, **311**, 317
- Cepa J., et al., 2000, in Iye M., Moorwood A. F., eds, Society of Photo-Optical Instrumentation Engineers (SPIE) Conference Series Vol. 4008, Optical and IR Telescope Instrumentation and Detectors. pp 623–631
- Cepa J., et al., 2003, in Iye M., Moorwood A. F. M., eds, Society of Photo-Optical Instrumentation Engineers (SPIE) Conference Series Vol. 4841, Instrument Design and Performance for Optical/Infrared Ground-based Telescopes. pp 1739–1749
- Chiappini C., Renda A., Matteucci F., 2002, *A&A*, **395**, 789
- Chini R., Wink J. E., 1984, *A&A*, **139**, L5
- Coc A., Angulo C., Vangioni-Flam E., Descouvemont P., Adah-chour A., 2005, *Nuclear Phys. A*, **752**, 522
- Cooke R. J., Fumagalli M., 2018, *Nature Astronomy*, **2**, 957
- Copetti M. V. F., Oliveira V. A., Riffel R., Castañeda H. O., Sanmartim D., 2007, *A&A*, **472**, 847
- D’Odorico S., Peimbert M., Sabbadin F., 1976, *A&A*, **47**, 341
- D’Odorico S., Cristiani S., Dekker H., Hill V., Kaufer A., Kim T., Primas F., 2000, in Bergeron J., ed., Society of Photo-Optical Instrumentation Engineers (SPIE) Conference Series Vol. 4005, Society of Photo-Optical Instrumentation Engineers (SPIE) Conference Series. pp 121–130
- Deharveng L., Peña M., Caplan J., Costero R., 2000, *MNRAS*, **311**, 329
- Delgado-Inglada G., Morisset C., Stasińska G., 2014, *MNRAS*, **440**, 536
- Domínguez-Guzmán G., Rodríguez M., Esteban C., García-Rojas J., 2019, arXiv e-prints, p. [arXiv:1906.02102](https://arxiv.org/abs/1906.02102)
- Drew J. E., Monguió M., Wright N. J., 2019, *MNRAS*, **486**, 1034
- Ekström S., et al., 2012, *A&A*, **537**, A146
- Esteban C., García-Rojas J., 2018, *MNRAS*, **478**, 2315
- Esteban C., Vilchez J. M., 1992, *ApJ*, **390**, 536
- Esteban C., Vilchez J. M., Smith L. J., Clegg R. E. S., 1992, *A&A*, **259**, 629
- Esteban C., Peimbert M., García-Rojas J., Ruiz M. T., Peimbert A., Rodríguez M., 2004, *MNRAS*, **355**, 229
- Esteban C., Bresolin F., Peimbert M., García-Rojas J., Peimbert A., Mesa-Delgado A., 2009, *ApJ*, **700**, 654
- Esteban C., Carigi L., Copetti M. V. F., García-Rojas J., Mesa-Delgado A., Castañeda H. O., Péquignot D., 2013, *MNRAS*, **433**, 382
- Esteban C., Mesa-Delgado A., Morisset C., García-Rojas J., 2016, *MNRAS*, **460**, 4038
- Esteban C., Fang X., García-Rojas J., Toribio San Cipriano L., 2017, *MNRAS*, **471**, 987

- Faúndez-Abans M., Maciel W. J., 1987, *A&AS*, **129**, 353
- Fernández-Martín A., Pérez-Montero E., Vílchez J. M., Mampaso A., 2017, *A&A*, **597**, A84
- Fernández V., Terlevich E., Díaz A. I., Terlevich R., Rosales-Ortega F. F., 2018, *MNRAS*, **478**, 5301
- Foster T., Brunt C. M., 2015, *AJ*, **150**, 147
- Froese Fischer C., Tachiev G., 2004, *Atomic Data and Nuclear Data Tables*, **87**, 1
- García-Rojas J., Esteban C., Peimbert M., Rodríguez M., Ruiz M. T., Peimbert A., 2004, *ApJS*, **153**, 501
- García-Rojas J., Esteban C., Peimbert A., Peimbert M., Rodríguez M., Ruiz M. T., 2005, *MNRAS*, **362**, 301
- García-Rojas J., Esteban C., Peimbert M., Costado M. T., Rodríguez M., Peimbert A., Ruiz M. T., 2006, *MNRAS*, **368**, 253
- García-Rojas J., Esteban C., Peimbert A., Rodríguez M., Peimbert M., Ruiz M. T., 2007, *Rev. Mexicana Astron. Astrofis.*, **43**, 3
- Georgy C., Ekström S., Meynet G., Massey P., Levesque E. M., Hirschi R., Eggenberger P., Maeder A., 2012, *A&A*, **542**, A29
- Gravity Collaboration et al., 2019, *A&A*, **625**, L10
- Grieve M. F. R., Ramsbottom C. A., Hudson C. E., Keenan F. P., 2014, *ApJ*, **780**, 110
- Hawley S. A., 1978, *ApJ*, **224**, 417
- Izotov Y. I., Thuan T. X., Lipovetsky V. A., 1994, *ApJ*, **435**, 647
- Izotov Y. I., Thuan T. X., Guseva N. G., 2014, *MNRAS*, **445**, 778
- Kingdon J., Ferland G. J., 1995, *ApJ*, **442**, 714
- Kisielius R., Storey P. J., Ferland G. J., Keenan F. P., 2009, *MNRAS*, **397**, 903
- Kubryk M., Prantzos N., Athanassoula E., 2015, *A&A*, **580**, A127
- Kunth D., Sargent W. L. W., 1983, *ApJ*, **273**, 81
- Kwitter K. B., 1984, *ApJ*, **287**, 840
- Lequeux J., Peimbert M., Rayo J. F., Serrano A., Torres-Peimbert S., 1979, *A&A*, **500**, 145
- Liu X.-W., Storey P. J., Barlow M. J., Danziger I. J., Cohen M., Bryce M., 2000, *MNRAS*, **312**, 585
- Lorenzo J., Simón-Díaz S., Negueruela I., Vilardell F., Garcia M., Evans C. J., Montes D., 2017, *A&A*, **606**, A54
- Luridiana V., Morisset C., Shaw R. A., 2015, *A&A*, **573**, A42
- Maciel W. J., 2001, *Ap&SS*, **277**, 545
- Marshall J. L., et al., 2008, in *Society of Photo-Optical Instrumentation Engineers (SPIE) Conference Series*. p. 54 ([arXiv:0807.3774](https://arxiv.org/abs/0807.3774)), doi:10.1117/12.789972
- Matteucci F., Chiappini C., 1999, in *Walsh J. R., Rosa M. R., eds, Chemical Evolution from Zero to High Redshift*. p. 83 ([arXiv:astro-ph/9812315](https://arxiv.org/abs/astro-ph/9812315))
- Mesa-Delgado A., Esteban C., García-Rojas J., Reyes-Pérez J., Morisset C., Bresolin F., 2014, *ApJ*, **785**, 100
- Moffat A. F. J., Fitzgerald M. P., Jackson P. D., 1979, *A&AS*, **38**, 197
- Osterbrock D. E., Ferland G. J., 2006, *Astrophysics of gaseous nebulae and active galactic nuclei*. 2nd. ed. Sausalito, CA: University Science Books
- Pagel B. E. J., Simonson E. A., Terlevich R. J., Edmunds M. G., 1992, *MNRAS*, **255**, 325
- Pasquali A., Perinotto M., 1993, *A&A*, **280**, 581
- Peimbert M., Costero R., 1969, *Boletín de los Observatorios Tonantzintla y Tacubaya*, **5**, 3
- Peimbert M., Serrano A., 1980, *Rev. Mex. Astron. Astrofis.*, **5**, 9
- Peimbert M., Torres-Peimbert S., 1977, *MNRAS*, **179**, 217
- Peimbert M., Rodríguez L. F., Torres-Peimbert S., 1974, *Rev. Mex. Astron. Astrofis.*, **1**, 129
- Peimbert M., Torres-Peimbert S., Rayo J. F., 1978, *ApJ*, **220**, 516
- Peimbert M., Torres-Peimbert S., Ruiz M. T., 1992, *RMxAA*, **24**, 155
- Peimbert A., Peimbert M., Luridiana V., 2002, *ApJ*, **565**, 668
- Peimbert A., Peña-Guerrero M. A., Peimbert M., 2012, *ApJ*, **753**, 39
- Peimbert A., Peimbert M., Luridiana V., 2016, *Rev. Mex. Astron. Astrofis.*, **52**, 419
- Planck Collaboration et al., 2018, *arXiv e-prints*, p. [arXiv:1807.06209](https://arxiv.org/abs/1807.06209)
- Podobedova L. I., Kelleher D. E., Wiese W. L., 2009, *Journal of Physical and Chemical Reference Data*, **38**, 171
- Porter R., Ferland G. J., MacAdam K., 2007, in *American Astronomical Society Meeting Abstracts*. p. 885
- Porter R. L., Ferland G. J., Storey P. J., Detisch M. J., 2012, *MNRAS*, **425**, L28
- Porter R. L., Ferland G. J., Storey P. J., Detisch M. J., 2013, *MNRAS*, **433**, L89
- Quiroza C., Rood R. T., Bania T. M., Balser D. S., Maciel W. J., 2006, *ApJ*, **653**, 1226
- Reid M. J., 1993, *ARA&A*, **31**, 345
- Rudolph A. L., Brand J., de Geus E. J., Wouterloot J. G. A., 1996, *ApJ*, **458**, 653
- Rudolph A. L., Fich M., Bell G. R., Norsen T., Simpson J. P., Haas M. R., Erickson E. F., 2006, *ApJS*, **162**, 346
- Russeil D., 2003, *A&A*, **397**, 133
- Russeil D., Adami C., Georgelin Y. M., 2007, *A&A*, **470**, 161
- Samal M. R., et al., 2010, *ApJ*, **714**, 1015
- Sawey P. M. J., Berrington K. A., 1993, *Atomic Data and Nuclear Data Tables*, **55**, 81
- Shaver P. A., McGee R. X., Newton L. M., Danks A. C., Pottasch S. R., 1983, *MNRAS*, **204**, 53
- Stasińska G., 1978, *A&A*, **66**, 257
- Stasińska G., Schaerer D., 1997, *A&A*, **322**, 615
- Stasińska G., Schaerer D., Leitherer C., 2001, *A&A*, **370**, 1
- Stock D. J., Barlow M. J., Wesson R., 2011, *MNRAS*, **418**, 2532
- Storey P. J., Hummer D. G., 1995, *MNRAS*, **272**, 41
- Storey P. J., Zeppen C. J., 2000, *MNRAS*, **312**, 813
- Storey P. J., Sochi T., Badnell N. R., 2014, *MNRAS*, **441**, 3028
- Talent D. L., Dufour R. J., 1979, *ApJ*, **233**, 888
- Tayal S. S., 2011, *ApJS*, **195**, 12
- Tayal S. S., Zatsarinny O., 2010, *ApJS*, **188**, 32
- Valardi M., Peimbert A., Peimbert M., Sixtos A., 2019, *ApJ*, **876**, 98
- Vílchez J. M., 1989, *Ap&SS*, **157**, 9
- Vílchez J. M., Pagel B. E. J., 1988, *MNRAS*, **231**, 257
- Vincenzo F., Miglio A., Kobayashi C., Mackereth J. T., Montalbán J., 2019, *A&A*, **630**, A125
- Wiese W. L., Fuhr J. R., Deters T. M., 1996, *J.Phys.Chem:Ref.Data*, Monograoh No. 7, Atomic transition probabilities of carbon, nitrogen, and oxygen : a critical data compilation. American Chemical Society, Washington, DC, and the National Institute of Standards and Technology (NIST)
- Zhang Y., Liu X. W., 2003, *A&A*, **404**, 545

## APPENDIX A: IONIC ABUNDANCES FOR EACH INDIVIDUAL He I LINE

In this Appendix we include four tables. Table A1 shows the  $\text{He}^+/\text{H}^+$  ratio for each individual He I line of the spectra analyzed in this work. In the second column we indicate the level state that produce each line, S for singlet and T for triplet. We also include the mean  $\text{He}^+/\text{H}^+$  ratio for each spectra. In Table A2 we give the list of individual He I lines used to derive the mean value of the  $\text{He}^+/\text{H}^+$  ratio adopted for each spectrum. In table Table A3 we include the results of the abundances of  $\text{He}^+/\text{H}^+$  estimated with the code He1io14. In Table A4 we include the ICFs used in each total abundance calculation.

**Table A1.** He<sup>+</sup>/H<sup>+</sup> ratios for each individual He I line of all the spectra used in this work

He I line (Å)	Level state	G2.4+1.4				
		A1	A2	A3	A4	A5
λ4471	T	-	10.865 ± 0.109	-	-	-
λ5876	T	10.808 ± 0.032	10.922 ± 0.029	10.817 ± 0.089	10.925 ± 0.025	11.003 ± 0.057
λ6678	S	10.720 ± 0.118	10.896 ± 0.036	-	10.867 ± 0.039	10.838 ± 0.093
Mean		10.800 ± 0.065	10.909 ± 0.016	10.817 ± 0.089	10.906 ± 0.031	10.937 ± 0.071
		M8	M16	M17	M20	M42
λ3614	S	10.844 ± 0.052	10.919 ± 0.052	10.934 ± 0.108	10.868 ± 0.057	10.947 ± 0.031
λ3965	S	10.849 ± 0.035	10.883 ± 0.017	10.938 ± 0.022	10.860 ± 0.017	10.925 ± 0.013
λ4026	T	-	-	-	-	-
λ4121	T	10.859 ± 0.027	11.013 ± 0.044	11.068 ± 0.056	10.598 ± 0.110	11.051 ± 0.019
λ4388	S	10.830 ± 0.013	10.886 ± 0.017	10.961 ± 0.026	10.826 ± 0.026	10.929 ± 0.009
λ4438	S	10.880 ± 0.044	10.817 ± 0.103	10.979 ± 0.109	10.938 ± 0.109	10.946 ± 0.035
λ4471	T	10.840 ± 0.013	10.893 ± 0.013	10.973 ± 0.013	10.850 ± 0.013	10.950 ± 0.005
λ4713	T	10.839 ± 0.014	10.900 ± 0.019	11.013 ± 0.026	10.825 ± 0.027	11.109 ± 0.011
λ4922	S	10.829 ± 0.013	10.883 ± 0.013	10.959 ± 0.013	10.862 ± 0.013	10.946 ± 0.005
λ5016	S	10.810 ± 0.013	10.864 ± 0.013	10.926 ± 0.013	10.849 ± 0.013	10.900 ± 0.006
λ5048	S	11.001 ± 0.018	11.057 ± 0.053	10.807 ± 0.048	10.925 ± 0.048	11.463 ± 0.011
λ5876	T	10.838 ± 0.013	10.903 ± 0.013	10.974 ± 0.013	10.855 ± 0.014	10.990 ± 0.014
λ6678	S	10.845 ± 0.013	10.895 ± 0.018	10.988 ± 0.017	10.862 ± 0.018	10.965 ± 0.026
λ7281	S	10.808 ± 0.016	10.900 ± 0.023	10.928 ± 0.022	10.885 ± 0.022	10.872 ± 0.038
λ9464	T	10.751 ± 0.022	10.690 ± 0.039	-	-	10.889 ± 0.065
Mean		10.838 ± 0.009	10.892 ± 0.009	10.967 ± 0.013	10.854 ± 0.009	10.946 ± 0.014
		NGC 2579	NGC 3576	NGC 3603	NGC 6888	
					A1	A2
λ3614	S	10.730 ± 0.052	10.927 ± 0.039	-	-	-
λ3965	S	10.904 ± 0.026	10.925 ± 0.013	10.895 ± 0.048	-	-
λ4026	T	10.962 ± 0.022	10.951 ± 0.013	-	-	11.191 ± 0.054
λ4121	T	11.050 ± 0.048	-	11.202 ± 0.086	-	11.600 ± 0.134
λ4388	S	10.961 ± 0.026	10.944 ± 0.013	11.025 ± 0.044	-	11.087 ± 0.068
λ4438	S	10.965 ± 0.070	11.003 ± 0.044	-	-	-
λ4471	T	10.964 ± 0.017	11.040 ± 0.009	11.021 ± 0.013	-	11.079 ± 0.014
λ4713	T	11.062 ± 0.023	11.086 ± 0.010	11.106 ± 0.032	-	-
λ4922	S	10.915 ± 0.017	10.938 ± 0.009	10.971 ± 0.018	-	11.143 ± 0.026
λ5016	S	10.898 ± 0.017	10.900 ± 0.009	10.876 ± 0.022	10.861 ± 0.122	11.080 ± 0.022
λ5048	S	-	-	-	-	11.176 ± 0.084
λ5876	T	11.011 ± 0.018	10.900 ± 0.018	10.999 ± 0.018	11.049 ± 0.036	11.161 ± 0.014
λ6678	S	10.943 ± 0.017	10.946 ± 0.026	10.974 ± 0.022	10.865 ± 0.073	11.151 ± 0.018
λ7281	S	-	10.953 ± 0.031	10.972 ± 0.029	-	10.986 ± 0.071
λ9464	T	10.949 ± 0.018	11.031 ± 0.048	11.226 ± 0.040	-	-
Mean		10.934 ± 0.026	10.941 ± 0.015	10.996 ± 0.027	10.977 ± 0.088	11.154 ± 0.014
		NGC 6888			NGC 7635	
		A3	A4	A5	A6	A1
λ4026	T	11.287 ± 0.070	11.240 ± 0.090	11.197 ± 0.065	11.206 ± 0.046	10.818 ± 0.137
λ4388	S	11.184 ± 0.131	-	11.128 ± 0.098	11.130 ± 0.107	10.879 ± 0.160
λ4471	T	11.156 ± 0.016	11.249 ± 0.045	11.235 ± 0.019	11.250 ± 0.020	10.818 ± 0.015
λ4713	T	11.068 ± 0.043	11.108 ± 0.049	11.138 ± 0.068	11.121 ± 0.043	10.872 ± 0.064
λ4922	S	11.215 ± 0.018	11.268 ± 0.030	11.237 ± 0.062	11.243 ± 0.034	10.833 ± 0.028
λ5016	S	11.174 ± 0.017	11.135 ± 0.022	11.194 ± 0.022	11.191 ± 0.022	10.881 ± 0.015
λ5048	S	11.122 ± 0.087	11.071 ± 0.121	11.103 ± 0.125	11.100 ± 0.068	10.953 ± 0.108
λ5876	T	11.237 ± 0.016	11.255 ± 0.013	11.235 ± 0.034	11.271 ± 0.012	10.889 ± 0.010
λ6678	S	11.227 ± 0.023	11.237 ± 0.019	11.257 ± 0.022	11.248 ± 0.028	10.878 ± 0.012
Mean		11.228 ± 0.013	11.251 ± 0.010	11.240 ± 0.013	11.259 ± 0.016	10.879 ± 0.005

This paper has been typeset from a  $\text{\TeX}/\text{\LaTeX}$  file prepared by the author.

Table A1. continued

He I line (Å)	Level state	NGC 7635				
		A2	A3	A4	A5	A6
$\lambda 4026$	T	-	$10.780 \pm 0.137$	$10.811 \pm 0.028$	$11.140 \pm 0.131$	-
$\lambda 4388$	S	-	-	$10.805 \pm 0.039$	-	-
$\lambda 4471$	T	$10.899 \pm 0.026$	$10.914 \pm 0.015$	$10.795 \pm 0.010$	$10.887 \pm 0.045$	$10.823 \pm 0.025$
$\lambda 4713$	T	$10.893 \pm 0.083$	$10.928 \pm 0.057$	$10.834 \pm 0.022$	-	-
$\lambda 4922$	S	$10.992 \pm 0.036$	$10.997 \pm 0.036$	$10.804 \pm 0.011$	$10.884 \pm 0.090$	$10.744 \pm 0.097$
$\lambda 5016$	S	-	-	$10.771 \pm 0.029$	$10.961 \pm 0.025$	$10.933 \pm 0.031$
$\lambda 5048$	S	$11.034 \pm 0.131$	$10.918 \pm 0.145$	$10.887 \pm 0.025$	-	-
$\lambda 5876$	T	$11.040 \pm 0.012$	$10.989 \pm 0.014$	$10.853 \pm 0.009$	$10.969 \pm 0.019$	$10.933 \pm 0.016$
$\lambda 6678$	S	$11.066 \pm 0.016$	$10.993 \pm 0.020$	$10.849 \pm 0.010$	$10.946 \pm 0.028$	$10.896 \pm 0.029$
$\lambda 7281$	S	-	$10.627 \pm 0.139$	$10.798 \pm 0.046$	$11.212 \pm 0.119$	-
Mean		$11.049 \pm 0.013$	$10.987 \pm 0.013$	$10.798 \pm 0.009$	$10.959 \pm 0.015$	$10.925 \pm 0.015$
		RCW 52	RCW 58	Sh 2-83	Sh 2-100	Sh 2-127
$\lambda 3965$	S	-	$11.484 \pm 0.069$	-	-	-
$\lambda 4026$	T	-	$11.297 \pm 0.068$	-	$10.973 \pm 0.033$	-
$\lambda 4388$	S	-	$11.186 \pm 0.108$	-	$10.923 \pm 0.038$	-
$\lambda 4471$	T	$10.761 \pm 0.147$	$11.226 \pm 0.018$	$10.907 \pm 0.040$	$10.986 \pm 0.013$	$10.746 \pm 0.039$
$\lambda 4713$	T	-	$11.134 \pm 0.144$	-	-	-
$\lambda 4922$	S	-	$11.186 \pm 0.066$	$10.895 \pm 0.037$	$10.989 \pm 0.024$	$10.801 \pm 0.026$
$\lambda 5016$	S	$10.827 \pm 0.141$	$11.220 \pm 0.016$	$10.883 \pm 0.049$	$10.919 \pm 0.056$	$10.808 \pm 0.014$
$\lambda 5048$	S	-	-	$10.999 \pm 0.078$	$10.980 \pm 0.070$	-
$\lambda 5876$	T	$10.819 \pm 0.024$	$11.210 \pm 0.016$	$10.972 \pm 0.014$	$11.042 \pm 0.024$	$10.832 \pm 0.012$
$\lambda 6678$	S	$10.840 \pm 0.038$	$11.257 \pm 0.020$	$10.902 \pm 0.021$	$11.008 \pm 0.035$	$10.790 \pm 0.015$
$\lambda 7281$	S	-	-	$10.778 \pm 0.046$	$10.897 \pm 0.047$	$10.561 \pm 0.072$
Mean		$10.825 \pm 0.009$	$11.217 \pm 0.008$	$10.899 \pm 0.007$	$10.984 \pm 0.015$	$10.799 \pm 0.008$
		Sh 2-128	Sh 2-152	Sh 2-209	Sh 2-212	Sh 2-288
$\lambda 4026$	T	-	$10.817 \pm 0.039$	-	-	$10.853 \pm 0.047$
$\lambda 4388$	S	-	$10.751 \pm 0.097$	-	-	-
$\lambda 4471$	T	$10.924 \pm 0.024$	$10.839 \pm 0.011$	-	$10.975 \pm 0.024$	$10.780 \pm 0.022$
$\lambda 4713$	T	-	$10.961 \pm 0.052$	-	-	-
$\lambda 4922$	S	$10.950 \pm 0.032$	$10.807 \pm 0.029$	-	$11.036 \pm 0.020$	$10.739 \pm 0.024$
$\lambda 5016$	S	$10.913 \pm 0.013$	$10.658 \pm 0.019$	$10.709 \pm 0.079$	$10.964 \pm 0.039$	$10.798 \pm 0.016$
$\lambda 5048$	S	$11.113 \pm 0.078$	$10.792 \pm 0.017$	-	-	$10.745 \pm 0.096$
$\lambda 5876$	T	$10.970 \pm 0.011$	$10.803 \pm 0.009$	$10.923 \pm 0.027$	$11.020 \pm 0.014$	$10.798 \pm 0.026$
$\lambda 6678$	S	$10.945 \pm 0.015$	$10.790 \pm 0.010$	$10.882 \pm 0.044$	$10.765 \pm 0.050$	$10.745 \pm 0.040$
$\lambda 7281$	S	$10.847 \pm 0.031$	$10.833 \pm 0.066$	$10.780 \pm 0.074$	-	$10.683 \pm 0.083$
Mean		$10.928 \pm 0.015$	$10.802 \pm 0.007$	$10.893 \pm 0.046$	$11.019 \pm 0.019$	$10.792 \pm 0.010$
		Sh 2-298	Sh 2-308	Sh 2-311		
$\lambda 3614$	S	-	-	$10.885 \pm 0.065$		
$\lambda 3965$	S	$10.819 \pm 0.102$	-	$10.905 \pm 0.018$		
$\lambda 4026$	T	$10.922 \pm 0.048$	-	$10.915 \pm 0.017$		
$\lambda 4121$	T	-	-	$10.926 \pm 0.039$		
$\lambda 4388$	S	$11.069 \pm 0.091$	-	$10.922 \pm 0.017$		
$\lambda 4438$	S	-	-	$10.963 \pm 0.065$		
$\lambda 4471$	T	$10.975 \pm 0.016$	-	$10.913 \pm 0.013$		
$\lambda 4713$	T	$10.949 \pm 0.079$	-	$10.919 \pm 0.018$		
$\lambda 4922$	S	$10.986 \pm 0.034$	-	$10.910 \pm 0.017$		
$\lambda 5016$	S	$10.740 \pm 0.074$	-	$10.892 \pm 0.013$		
$\lambda 5048$	S	-	-	$11.040 \pm 0.044$		
$\lambda 5876$	T	$10.969 \pm 0.017$	$11.199 \pm 0.047$	$10.911 \pm 0.018$		
$\lambda 6678$	S	$11.020 \pm 0.037$	$11.202 \pm 0.077$	$10.916 \pm 0.017$		
$\lambda 7281$	S	$10.617 \pm 0.101$	-	$10.909 \pm 0.022$		
$\lambda 9464$	T	-	-	$10.985 \pm 0.035$		
Mean		$10.971 \pm 0.017$	$11.200 \pm 0.062$	$10.914 \pm 0.006$		

**Table A2.** List of lines used for the calculation of the mean  $\text{He}^+/\text{H}^+$  ratio for each spectra.

Object	Zone	Lines used
G2.4+1.4	A1	5876, 6678
	A2	4471, 5876, 6678
	A3	5876
	A4	5876, 6678
	A5	5876, 6678
M8		3614, 3965, 4121, 4388, 4438, 4471, 4713, 4922, 5876, 6678
M16		3614, 3965, 4388, 4438, 4471, 4713, 4922, 5876, 6678, 7281
M17		3614, 3965, 4388, 4438, 4471, 4922, 5876, 6678
M20		3614, 3965, 4388, 4438, 4471, 4922, 5016, 5876, 6678
M42		3614, 3965, 4388, 4438, 4471, 4922, 5876, 6678, 7281, 9464
NGC 2579		3965, 4026, 4388, 4438, 4471, 4922, 5016, 6678, 9464
NGC 3576		3614, 3965, 4026, 4388, 4438, 4922, 6678, 7281, 9464
NGC 3603		4121, 4388, 4471, 4922, 5876, 6678, 7281
NGC 6888	A1	5016, 5876, 6678
	A2	4026, 4388, 4922, 5048, 5876, 6678
	A3	4026, 4388, 4922, 5876, 6678
	A4	4026, 4471, 4922, 5876, 6678
	A5	4026, 4471, 4922, 5876, 6678
	A6	4026, 4471, 4922, 5876, 6678
RCW 52		4471, 5016, 5876
RCW 58		4388, 4471, 4922, 5016, 5876
NGC 7635	A1	4026, 4388, 4713, 5016, 6678
	A2	5048, 5876, 6678
	A3	4713, 4922, 5048, 5876, 6678
	A4	4026, 4388, 4471, 4922, 5016, 7281
	A5	4922, 5016, 5876, 6678
	A6	5016, 5876, 6678
Sh 2-83		4471, 4922, 5016, 6678
Sh 2-100		4026, 4471, 4922, 5016, 5048, 6678
Sh 2-127		4922, 5016, 6678
Sh 2-128		4471, 4922, 5016, 6678
Sh 2-152		4026, 4922, 5048, 5876, 7281
Sh 2-209		5876, 6678, 7281
Sh 2-212		4922, 5016, 5876
Sh 2-288		4471, 5016, 5048, 5876
Sh 2-298		4026, 4388, 4471, 4713, 4922, 5876
Sh 2-308		5876, 6678
Sh 2-311		3614, 3965, 4026, 4121, 4388, 4471, 4713, 4922, 5876, 6678, 7281

**Table A3.** Results of HeIio14 code: He<sup>+</sup>/H<sup>+</sup> ratios, minimal  $\chi^2$  and  $T_e(\text{OII}+\text{OIII})$ .

Object	Zone	He <sup>+</sup> /H <sup>+</sup>	$\chi^2$	$T_e(\text{OII}+\text{OIII})$ (K)
G2.4+1.4	A1	10.800 ± 0.132	0.4824	8300
	A2	10.913 ± 0.062	0.2778	9900
	A3	10.823 ± 0.025	0.0001	13200
	A4	10.911 ± 0.056	1.5670	10800
	A5	10.955 ± 0.104	2.1964	9400
M8		10.835 ± 0.006	3.1286	8300
M16		10.892 ± 0.005	1.8101	8200
M17		10.951 ± 0.010	1.7033	8100
M20		10.849 ± 0.006	5.6603	8200
M42		10.937 ± 0.005	10.4708	8600
NGC 2579		10.932 ± 0.007	9.9796	9100
NGC 3576		10.940 ± 0.005	6.4027	8500
NGC 3603		10.997 ± 0.008	11.1381	9200
NGC 6888	A1	10.938 ± 0.061	6.3886	9000
	A2	11.135 ± 0.010	3.6936	8100
	A3	11.211 ± 0.024	1.1789	8200
	A4	11.248 ± 0.017	1.1147	9800
	A5	11.215 ± 0.031	0.4958	9700
	A6	11.222 ± 0.029	1.1959	9300
RCW 52		10.797 ± 0.135	0.1317	7000
RCW 58		11.218 ± 0.011	0.5340	5700
NGC 7635	A1	10.876 ± 0.010	0.2989	7800
	A2	11.049 ± 0.061	3.73	8000
	A3	10.979 ± 0.036	0.20	7900
	A4	10.794 ± 0.009	1.4294	8900
	A5	10.959 ± 0.016	2.2715	7700
	A6	10.926 ± 0.016	1.4503	7500
Sh 2-83		10.894 ± 0.026	0.0529	10500
Sh 2-100		10.969 ± 0.019	0.9411	8300
Sh 2-127		10.804 ± 0.010	0.3323	9800
Sh 2-128		10.927 ± 0.010	0.4683	10200
Sh 2-152		10.794 ± 0.008	0.9671	8100
Sh 2-209		10.855 ± 0.034	0.7623	10700
Sh 2-212		11.003 ± 0.017	1.8543	9200
Sh 2-288		10.792 ± 0.011	0.8347	9400
Sh 2-298		10.967 ± 0.016	2.5547	11700
Sh 2-308		11.177 ± 0.056	0.0046	16300
Sh 2-311		10.909 ± 0.006	0.9385	9200

**Table A4.** ICF values.

Object	PTP77	ICF(He) scheme		
		ZL03	KS83	B09
G2.4+1.4			-	
M8	1.33 ± 0.09	1.15 ± 0.02	1.23 ± 0.07	1.82 ± 0.36
M16	1.59 ± 0.21	1.38 ± 0.08	1.24 ± 0.07	1.23 ± 0.27
M17	1.06 ± 0.02	1.04 ± 0.01	1.05 ± 0.01	1.05 ± 0.09
M20	1.54 ± 0.16	1.30 ± 0.06	1.27 ± 0.07	1.74 ± 0.46
M42	1.08 ± 0.04	1.04 ± 0.02	1.04 ± 0.02	1.02 ± 0.09
NGC 2579	1.16 ± 0.05	1.09 ± 0.02	1.10 ± 0.04	1.10 ± 0.18
NGC 3576	1.13 ± 0.04	1.08 ± 0.02	1.09 ± 0.02	1.05 ± 0.10
NGC 3603	1.03 ± 0.01	1.02 ± 0.01	1.02 ± 0.01	1.03 ± 0.13
NGC 6888			-	
NGC 7635 A1	1.37 ± 0.17	1.23 ± 0.09	1.22 ± 0.08	1.32 ± 0.46
NGC 7635 A2	1.09 ± 0.08	1.05 ± 0.04	1.09 ± 0.07	1.28 ± 0.96
NGC 7635 A3	1.10 ± 0.10	1.05 ± 0.05	1.10 ± 0.08	1.39 ± 1.31
NGC 7635 A4	1.30 ± 0.10	1.15 ± 0.06	1.24 ± 0.05	1.98 ± 0.82
NGC 7635 A5	1.20 ± 0.23	1.12 ± 0.13	1.15 ± 0.14	1.21 ± 1.05
NGC 7635 A6	1.21 ± 0.28	1.12 ± 0.15	1.16 ± 0.18	1.25 ± 1.32
RCW 52	1.39 ± 0.49	1.22 ± 0.17	1.27 ± 0.36	2.12 ± 2.47
RCW 58	1.15 ± 0.10	1.06 ± 0.03	1.17 ± 0.12	1.94 ± 1.33
Sh 2-83	1.04 ± 0.02	1.05 ± 0.02	1.02 ± 0.01	1.25 ± 0.45
Sh 2-100	1.06 ± 0.02	1.04 ± 0.01	1.05 ± 0.01	1.04 ± 0.13
Sh 2-127	1.39 ± 0.12	1.16 ± 0.04	1.28 ± 0.08	1.47 ± 0.63
Sh 2-128	1.19 ± 0.07	1.12 ± 0.03	1.12 ± 0.03	1.07 ± 0.17
Sh 2-152	1.31 ± 0.07	1.09 ± 0.02	1.27 ± 0.05	3.35 ± 0.64
Sh 2-209	1.22 ± 0.30	1.17 ± 0.16	1.10 ± 0.14	1.01 ± 0.08
Sh 2-212	1.28 ± 0.40	1.16 ± 0.15	1.20 ± 0.30	1.50 ± 1.60
Sh 2-288	1.37 ± 0.25	1.18 ± 0.11	1.22 ± 0.12	1.60 ± 1.03
Sh 2-298	1.91 ± 0.53	1.95 ± 0.20	1.15 ± 0.06	1.46 ± 0.40
Sh 2-308	1.05 ± 0.08	1.06 ± 0.06	1.03 ± 0.04	1.16 ± 1.09
Sh 2-311	1.47 ± 0.14	1.33 ± 0.05	1.23 ± 0.07	1.20 ± 0.18